CHALMERS
UNIVERSITY OF TECHNOLOGY

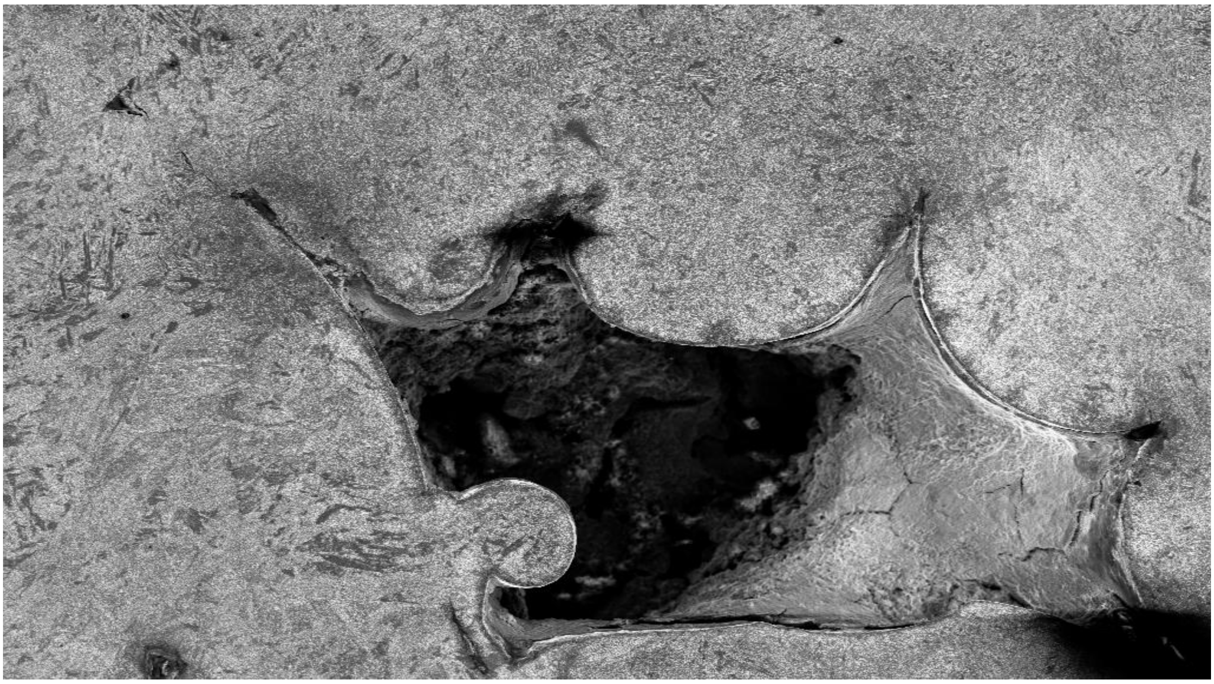

Improving Build Rate of Low Alloy Steels Produced by Laser Powder Bed Fusion:

Influence of layer thickness on processability

Master's thesis in materials engineering master's program

Rasmus Martin Gunnerek

DEPARTMENT OF INDUSTRIAL AND MATERIAL SCIENCE

CHALMERS UNIVERSITY OF TECHNOLOGY
Gothenburg, Sweden 2020
www.chalmers.se

Abstract

One of the largest issues with laser powder bed fusion (L-PBF) is the limited number of alloys that have been qualified for the process. This is especially true for low alloyed steels, as the carbon content can adversely affect processability by increasing number of defects as cracking and/or porosity. Previous work in the Powder Metallurgy and Additive Manufacturing group at Chalmers in the frame of CAM^2 established a set of processing windows for two low alloy steels (4130 & 4140) that could produce of defect-free, high density components (>99.8%). The current work focused on increasing the build rate of these alloys by varying the layer thickness. Specimens were produced at layer thicknesses of 40 μm and 60 μm, across surface energy densities (SED) of 2.4 to 3.8 J/mm^2. From this investigation, a 40 μm layer thickness yielded a wider processing window in comparison to a 60 μm layer thickness. Examinations of the microstructure revealed a greater number of lack-of-fusion defects at a larger layer thickness, which were the cause of this narrower process window. The melt pool depth at a 60 μm layer thickness was 100-240 μm, indicating that this lack of fusion porosity stemmed from instabilities within the powder bed. It was also found that an increased layer thickness yielded a lower hardness. This was connected to a more pronounced in-situ tempering that occurred at a 60 μm layer thickness. As a result, processing windows for 4130 and 4140 alloys, at layer thicknesses of 40 and 60 μm, were established, allowing to produce defect free, high density (>99.8%) components. Increasing layer thickness allowed to improve the build rate of these materials by up to ~165% in comparison to the previously developed parameters.

Acknowledgements

There are several people without whom this project would not have been possible. First, I would like to thank my supervisor William Hearn (PhD. Student in Additive Manufacturing at Chalmers University of Technology) for the numerous hours of interesting discussions as well as guidance in the lab. I also want to thank my examiner Professor Eduard Hryha for giving me the opportunity to work within CAM^2 a project in the forefront of research and development of powder based additive manufacturing.

Table of contents

1. Introduction

Laser powder bed fusion (L-PBF) is one of the most prominent additive manufacturing (AM) processes. Process utilizes a laser heat source, navigated by a computer aided design, to selectively fuse metal powder in a layer by layer fashion. Compared to conventional manufacturing, the geometrical freedom, unique properties and ability to manufacture customized complex components, have gained interest from several industries such as aerospace, medical and automotive [1]. Two decades of development have contributed to some certifications of alloy systems (e.g. titanium, Ni-base super alloys and stainless steel). However, the number of certified alloys remains rather limited. This is due to the complexity of L-PBF. There are well over 100 process related parameters and minor changes can significantly alter the process conditions i.e. melt pool stability, cooling rates, heat distribution, etc. The effect of process parameters on the print quality of a specific material is commonly based on trial and error which requires time and effort to understand. The limited alloys available leaves large gaps in potential applications that could benefit from the unique capabilities of the technology [1], [2].

In structural engineering, steel is one of the most used materials. However, like in welding, carbon have a poor influence on processing as it increases the susceptibility to cracking and other defects during L-PBF. Namely, increased carbon content promotes the formation of the brittle martensitic phase which in combination with the high cooling rates generate large residual stresses. Therefore, studies on steels have focused on alloys with low carbon contents or high alloy contents such as stainless steels and tool steels. Recently, the advances in technology have seen increased interest in steels with higher carbon content. Process controlling features such as preheating of the build plate are promising steps towards decreasing residual stresses developed by rapid melting/cooling and the presence of martensite during the process. [1], [2]

Only a handful studies have been conducted on low alloy steels for L-PBF, e.g. 4140 [3], [4], [5], 4130 [6] and 4340 [7], [8]. Conventionally, low alloy steels can be tailored by various heat treatments to achieve high strengths and good corrosion resistance, thus, finding its use in several demanding applications such as thin walled pressure vessels [9]. In Figure 1 a), a classical Ashby plot (conventional steels) provides a good representation of the gap in properties that low alloy steels would fill if added to the portfolio of ferrous L-PBF materials.

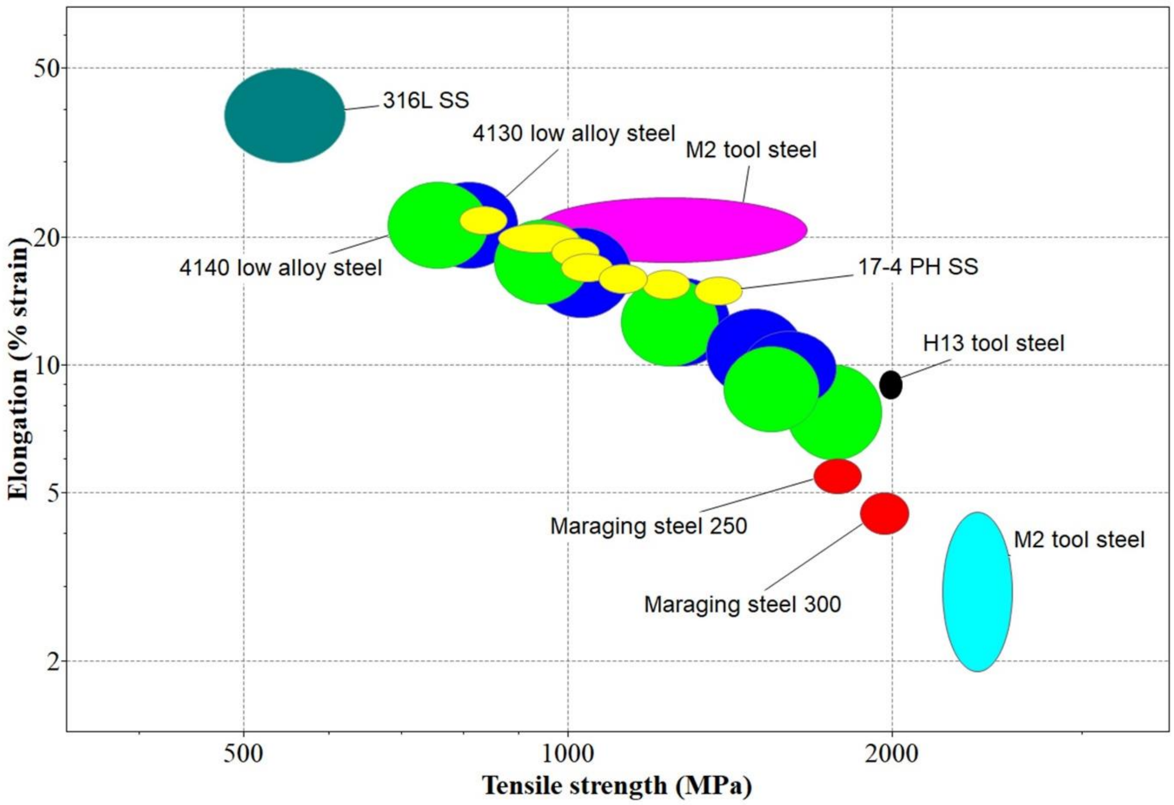

Figure 1. Ashby plot illustrating mechanical properties of conventionally manufactured ferrous alloys currently under development for L-PBF.

In this work, the printability of 4140 & 4130 alloys is investigated as a continuation of the research and development of ferrous alloys at the Powder Metallurgy and Additive Manufacturing group at Chalmers in the frame of CAM^2. Building on previously established processing windows, this project aims to improve the build rate of said alloys by increasing the layer thickness and the research question are formulated as follows:

- What process parameters are important when varying layer thickness?
- What is the influence of layer thickness on the processing window
- How does the formation of defects change when the layer thickness is changed?
- How do the melt pool characteristics change with layer thickness?
- How does varying the layer thickness vary the build rate?

2. Background

2.1 Current state of the art of L-PBF AM technologies

Through the last two decades significant development has occurred in additive manufacturing (AM), moving from porous rapid prototyping to a process that can achieve high density components that are suitable for various applications, such as medical and aerospace. Currently, one of the most prominent AM methods is laser powder bed fusion (L-PBF), where metal powder is melted by a laser in a layer-upon-layer fashion to achieve a 3D structure. This unique method of manufacturing has gained large interest from industry since light weight and complex structures can be built on demand, cutting lead time, without the need of conventional material removal processes [1], [2].

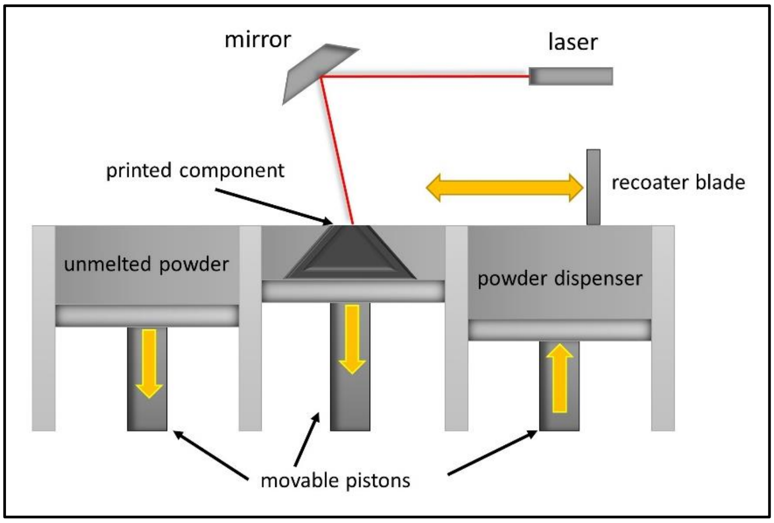

Figure 2. General schematic of Laser Powder Bed Fusion inspired by [29].

In Figure 2, a schematic of the L-PBF process is illustrated. Initially metal powder is evenly distributed onto a building platform, by a roller or recoater blade, which is lowered to a certain distance corresponding to the powder layer thickness. The powder is then selectively melted by a laser source. Upon completion of the current layer the build-platform is lowered vertically, and fresh powder is distributed by the feeder. These steps are repeated until the final component is achieved [1], [2], [10].

L-PBF is performed in a controlled inert atmosphere to prevent unwanted reactions between the built material, feedstock material and surrounding gases. Therefore, a constant supply of inert gas is typically supplied in order to keep the oxygen levels below 0.1%. Potential contamination of the components, from processing by-products, is also prevented by the gas flow [10].

During manufacturing, L-PBF components experience intricate thermal cycles leading to evolution of metastable phases. While locally scanning the surface, rapid melting occurs as the powder absorbs the energy of the laser and quickly solidifies as the laser passes reaching cooling rates up to $10^6\,^{\circ}\mathrm{C}\cdot\mathrm{s}^{-1}$ [11]. Consequently, steep temperature gradients are generated through the part leading to very fine grain sizes and the rapid solidification can lock phases in metastable state due to insufficient time for diffusion. To add to the complexity, the same region will be re-heated or re-melted once a new layer or laser track is exposed to the laser. This very nature makes L-PBF microstructures difficult to predict as the slightest change of process parameters can alter the thermal state and thus the resulting part density and microstructural evolution [1], [2].

According to Fayazfar et al. [2], three trends regarding microstructure morphology have been found in studies of L-PBF. Depending on the relationship between temperature gradient and solidification velocity, either equiaxed, columnar or a mixture of equiaxed and columnar grains is formed. However, as the heat source operates perpendicular to the build plate the thermal gradient is higher in the build direction, mainly generating columnar grains. Furthermore, heat dissipation is less in the x-y direction yielding anisotropy in microstructure. Compared to conventional microstructures, the combination of the earlier mentioned thermal conditions, e.g. fine localized melting and rapid cooling, yields finer grains and a small heat effected zone in L-PBF [2].

2.2 Process parameters

One of the greatest challenges regarding L-PBF is the vast number of parameters influencing the quality of components. According to several studies, there are well over 100 process related parameters that can affect the process [11], [12]. In Figure 3, an illustration of the most important process parameters, e.g. laser power, layer thickness, hatch spacing, and scan speed is presented alongside geometrical representations of the melt pool. These parameters are altered by experiments to achieve high density, low porosity, allowable material properties at high build rates [11]. In the following sections the impact of the main process parameters is introduced separately.

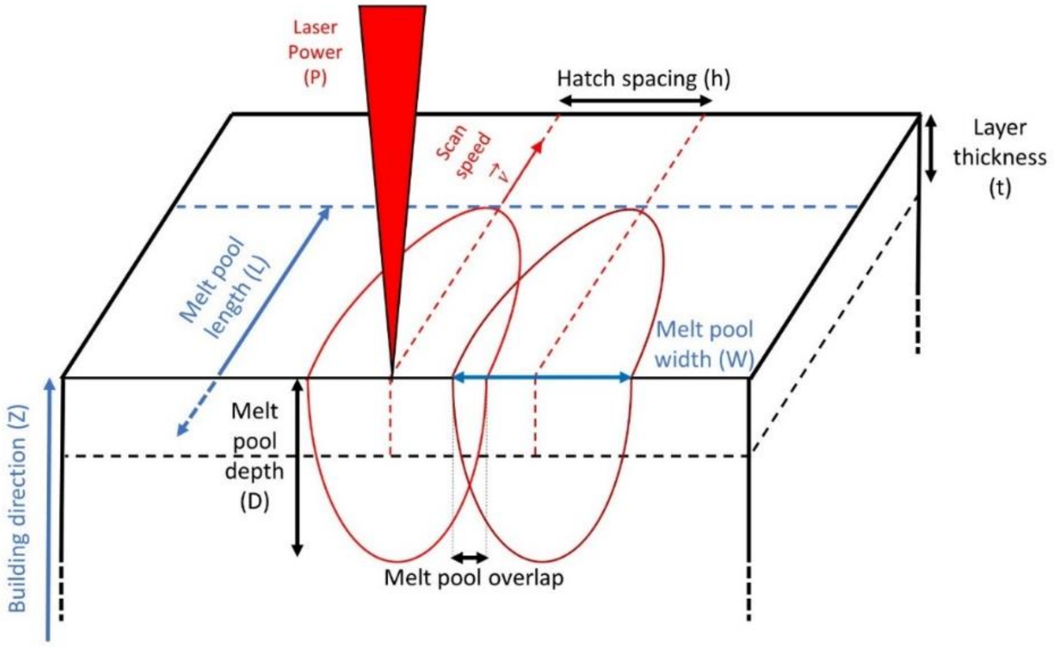

Figure 3. Schematic of process parameters and melt pool characteristics, inspired by [12].

2.2.1 Laser power and laser source characteristics

The laser power, measured in Watts (W), is one of the most important parameters during L-PBF as it governs the amount of energy delivered to the feedstock material. The range in which the laser power can be altered is machine dependent, generally between 10-1000 W [1], [10]. The laser beam spot size is fine, varying between different systems, typically 50-100 µm. The small spot size enables fine resolution of L-PBF prints. It is important to keep in mind the used spot size as it can vary the energy density experienced by the powder bed even if the laser power is the same. As a smaller spot size delivers higher energy per unit area or volume, at the same laser power [1].

2.2.2 Scan speed

The time in which a specific region of the powder is exposed to laser is directly connected to the scan speed. The scan speed influences heat accumulation, thermal gradient and melt pool characteristics. At a constant laser power, increasing the scan speed tends to alter the size and geometry of the melt pool. Subsequently, the melt pool length (L) increases in proportion to the melt pool width (W) and depth (D) as the powder bed is exposed to the laser during a shorter time [1], [10].

2.2.3 Hatch spacing

To ensure proper overlap of subsequent melt tracks, a reasonable hatch spacing should be used. Gaps between solidified tracks will lead to insufficient fusion and cause intra-layer porosity called lack-of-fusion [1], [2], [6]. Studies imply that choosing a hatch spacing smaller than the spot size of the laser or width of the melt pool is a good guideline. However, it is also proven to be a rather conservative assumption as the melt pool width can be larger than the spot size as it is governed by the laser power and scan speed [6].

2.2.4 Layer thickness

Layer thicknesses between 20 and 40 μm are generally used in L-PBF in order to achieve good geometrical accuracy and surface quality. However, increasing the layer thickness would heavily increase the build rates of L-PBF as it would decrease the number of layers required to build [13], [14]. The layer thickness is observed to effect the powder bed density due to variations in powder spreading. Larger particles can be removed by the recoater when the layer thickness is smaller than the D90 size of the particle size distribution [12]. According to Letenneur et al. [12], this phenomenon alters physical properties such as the thermal conductivity of the powder bed which leads to altered heat distribution during operation.

2.2.5 Combining process parameters

In order to compare the performance of printed materials, based on different combinations of process parameters, attempts have been made to identify a single parameter. The commonly used volumetric energy density (VED), see equation 1, is defined as a function of laser power (P), scan speed (v), hatch spacing (h) and layer thickness (t). VED describes the total heat input experienced by the powder per unit volume and is shown to correlate with the density evolution of L-PBF components [15]. Thus, VED enables a simplified representation of regions in processing space where high density parts are obtainable.

$$VED = \frac{\mathrm{P}}{\mathrm{v*h*t}} \quad [\mathrm{J/mm^3}] \tag{1}$$

Bertoli et al. [15] investigated the reliability of VED to encapsulate density evolution of single melt tracks. While VED was found good at predicting melt pool width it failed to explain melt pool shape and morphology. Even though the same VED was used, the formed melt track varied significantly in stability because of the inability to account for complex physics driving the kinetics of a single melt pool i.e. mass and heat flow to the surrounding [15]. Therefore, VED should be used with caution if used as the sole process parameter, when comparing between different alloys and the best results are gained by altering a minimum of parameters.

Other studies illustrated their results in terms surface energy density (SED) by combining laser power (P), scan speed (v) and beam diameter (d). They found that by using a 2D representation of supplied energy, decent predictions of melt pool depth and width was achieved as both the melt pool depth and width increased with increased surface energy density [4], [16].

$$SED = \frac{\mathrm{P}}{\mathrm{v*d}} \ [\mathrm{J/mm^2}] \tag{2}$$

An even more simplified parameter is the linear energy density (LED) which solely contains the relationship between laser power and scan speed. The main usage of LED is when conducting single track experiments where the interest lies in understanding how it captures melt track stability and alters melt pool dimensions (see Figure 3) [17].

$$LED = \frac{\mathrm{P}}{\mathrm{v}} \quad [\mathrm{J/mm}] \tag{3}$$

As illustrated in this chapter, the combined process parameters are usually based on laser power and scan speed due to the stated connection between energy supplied to the powder and the evolution of density during L-PBF. However, one should be aware that the mentioned parameters have limitations [15]:

1. The same LED, SED and VED can be achieved by multiple combinations of input parameters and the possible combinations increases with the parameters used (adding dimensions i.e. 1D, 2D and 3D)
2. As thermal quantities the oversimplification fails to explain complex phenomena e.g. mass and heat transfer within the melt pool.

2.3 Influence of L-PBF process parameters on defect formation

The complexity of L-PBF makes it prone to process related defects. There are various types of defects induced by intricate mechanisms and phenomena that occur during L-PBF processing. As defects are detrimental to mechanical properties, their origin and evolution in relation to process parameters are essential [1], [2], [10]. According to Sola and Nouri [18], there is a distinction between process induced and powder induced defects. Powder related parameters as e.g. packing density, particle size distribution and powder shape, may influence the susceptibility of different defects. It is said that spherical powders with a good size distribution are beneficial and contribute to higher densities of parts. All though these conditions are met, defects such as gas porosities can be present within powder particles as a result of entrapped gas during powder fabrication [19]. Process related defects are considered as defects that can be directly correlated to the used process parameters, i.e. laser power, scan speed, hatch spacing, etc. [19]. In the following sections the formation of such defects will be discussed in more details.

2.3.1 Lack-of-fusion

Lack-of-fusion is the lack of cohesion between the two adjacent melt tracks due to improper melting, characterized by trapped un-melted powder and its irregular shape, and is mainly located in between layers [19]. Compared to other defects, these porosities are large and have a sharp corner, thus acting as stress concentrations which leaves the component vulnerable to cracking [19]. In order to avoid lack-of-fusion between layers, a rule of thumb is that the energy delivered to the powder should result in a melt pool depth, equal or larger than the layer thickness ($D/t>1$) to ensure proper bonding of layers. This is generally controlled by increasing the laser power or decreasing the scan speed [1], [10]. Lack-of-fusion can also develop in between subsequent melt tracks due to poor overlapping of melt pools, leaving long sharp lines parallel to the scan direction. Lack-of-fusion between melt tracks can be prevented by decreasing hatch spacing to ensure sufficient overlap or by increasing the energy density to increase the melt pool width [10].

2.3.2 Balling

Balling is an effect of Plateau-Rayleigh capillary instability occurring when the melt pool length (L) increases to a certain threshold in relation to its width (W). The melt track breaks up into spheres in order to minimize its surface energy, leaving discontinuities in the melt track [17], [19]. Balling mainly occurs at high scan speeds as the melt pool narrows and increase in length. In addition, the high temperature in L-PBF lowers the overall viscosity of the melt, decreasing the wettability and further promoting the balling phenomena. To prevent balling, optimized laser power and scan speeds are essential to keep the length/width ratio low and stable. Therefore, single track experiments are often performed to identify LED ranges in which the melt pools are continuous early in process optimization. Balling can cause various issues during the process, large spheres can inhibit proper powder spreading of a new layer as well as leaving porosities and rough surfaces [17], [20].

2.3.3 Keyhole formation

At high laser powers the generated melt pool can become deep and narrow, inducing a third type of defect called keyhole porosity. The steep thermal gradient in such melt pools leads to evaporation of elements with low melting temperature. The vapor generated cannot escape the deep melt pool leaving voids behind after solidification. Keyholes are often semi-spherical and located at the bottom of melt pools. There have also been observations of keyholes developing at the end or start of laser tracks. When the laser beam suddenly changes direction thermal instabilities of the melt can induce a keyhole [19]. The risk of keyhole formation is lowered either by decreasing the laser power or increasing the scan speed.

2.3.4 Spattering

Unstable melt pools can lead to ejection of powder droplets on to the powder bed called spattering or splashing. The process instability creates discontinuous melt tracks and ejected powder has been observed to leave protrusions or valleys of unmelted regions on the powder substrate. When a subsequent layer is being fused these valleys can remain unmelted, causing large pores, as the penetration needs to be larger than one layer [21].

2.3.5 Cracks

Cracking is another category of defects that occur in L-PBF and share similarities to cracks found in welding. The higher cooling rates in L-PBF (up to 10^6 °C·s^{-1}) lead to the development of large amounts of residual stress which could make the material vulnerable towards cold cracking [1], [5]. Cold cracking is especially observed in steels of high carbon content due to the increased formation of the hard and brittle martensitic phase. The risk of cold cracking increases with the carbon equivalent which correlates to the hardenability of the material [2]. In order to decrease the residual stresses and enable prints of higher carbon content, preheating of the build plate is used to lower the thermal gradients during L-PBF [22].

Solidification cracks is an additional crack occurring in L-PBF. These are observed in the direction of grain boundaries which occurs due to significant contraction of solidifying melt pools. The temperature of the melt pool is higher than that of the previous layer which is hindered by the surrounding material to compensate for the contraction leading to large tensile stresses. Further, if the stress surpasses the yield strength of the material cracking may occur [1].

2.4 Printability and process optimization

Due to the intricate conditions of L-PBF, only a few metal alloys such as titanium-based alloys, stainless and tool steels, nickel- and aluminum-based alloys, etc., are optimized to achieve the full density required for industrial use [10]. Approving a certain alloy is time-consuming as full knowledge of the connection between powder material, process parameters, microstructure and mechanical properties are essential for consistent defect-free part production. Within conventional manufacturing, weldability identifies some materials more easily welded than others, however, in AM the printability of alloys is traditionally established by trial and error of the various processing parameters [1].

2.4.1 Framework of process optimization and strategies

In literature, two trends can be observed regarding the main focus of alloy optimization in L-PBF [2]:

1. Establishing a printable region in terms of process parameters where fully dense parts are possible at a maximized build rate.
2. Understanding the connection between process parameters and the microstructural evolution as well as how these factors affect mechanical properties.

However, the approach in which these fields are studied, differs in literature and the trends mentioned in each often overlap.

Starting with a wide range of laser power and scan speed combinations (LED) can be beneficial as it governs melt pool characteristics and process stability, helping understand the evolution of defects such as lack-of-fusion, keyhole porosities and balling [23]. Therefore, early in the optimization process, single track experiments are conducted to establish LED ranges that produce continuous melt tracks. The ranges of melt track widths (W) can provide a good guide towards what hatch spacing should be used. In addition, the melt pool depth (D) provides indications towards the selection of layer thickness. Single track experiments require very low amounts of powder to perform and can narrow the range of parameter used for the main printing. In other words, starting with single tracks and solely varying two parameters is useful before adding the complexity of several tracks overlapping as well as the intricacy of new layer/previous layer interactions [1], [10], [17].

With either the knowledge from single track experiments or results gained in the literature, the next step of alloy optimization is to print multiple cubes in ranges of VED. It is based on designing experiments by organizing various combinations of scan speed, hatch spacing and laser power [12]. The performance of each parameter set is then characterized in terms of density and mechanical properties. A consideration is made regarding the impact of each parameter and the gained knowledge sets the foundation of new experiments for further optimization. This trial and error approach have been shown to deliver pleasant results, however, it can be costly and inefficient as numerous prints and characterizations are needed [12].

On the other hand, several studies imply that the maturity of L-PBF is to move from a trial and error-based, to a prediction-based approach utilizing numerical simulation and modelling of process parameters, material parameters and melt pool characteristics [12], [21], [23]. By using prediction models, efficient guidelines in choosing process parameter can decrease the costs and time required by trial and error. However, there is a challenge in developing accurate simulations without too much computing load. Therefore, it is necessary to find a balance between model assumptions and computational workload without losing prediction accuracy [23].

2.4.2 Build rate

A great challenge of L-PBF systems is the low build rate. This stems from the rather limited delivery rate of powder, small layer thickness and low scan speeds [1], [2]. Sun et al. [24], investigated whether the build rate of 316L SS could be improved by using a laser power of 380 W compared to 100 W, as commonly used. They found that the higher laser power allows faster scanning speeds, while still obtaining densities above 99%. Consequently, the build rate was increased by approximately 72%, thus, indicating the importance of laser power on improving build rate of L-PBF alloys. In another study on maraging steel, layer thickness is emphasized to be the most essential process parameter influencing the build rate as an increase in layer thickness by 66% increases the build rate by 40% [25].

Kniepkamp et al. [14] divided build time into two parts, namely the main and idle build time. The main build time was defined as the sequence in the process where the laser is in operation and melting the powder across the surface. This sequence, what many consider as the build rate, is defined by the combination of scan speed, layer thickness and hatch spacing (cm^3/h) [12], [14]. On the other hand, the idle time is the time required to deposit new powder in between subsequent runs. Out of the main processing parameters the layer thickness is the only one that directly influence the total idle time. As an increased layer thickness decreases the total number of layers required to build a certain volume of material. This is why many works have focused on increasing the layer thickness when trying to optimize the build rate [12], [14].

2.5 Current state of the art in the L-PBF of low alloy steels

In engineering, steel is one of the commonly utilized materials in structural applications and thus a material of great interest for L-PBF [10]. However, the poor influence of carbon on processability, including increased susceptibility to cracking, defects and porosity, is not beneficial. In review articles on the current state AM of ferrous alloys [2], [26], it is presented that the area of L-PBF steels have focused on alloys with limited amount of carbon and high alloying contents e.g. maraging steel, tool steels and austenitic stainless steels. In austenitic stainless steels such as 316L the high nickel and low carbon content suppresses the diffusionless martensitic transformation which makes it easier to process by L-PBF. However, the previously mentioned alloys leave a gap in potential structural applications for L-PBF steel alloys as they either lack strength or cost efficiency due to a high alloying content [2].

Low alloy steels is a type of ferrous alloys where the small addition of alloying elements (up to 12 wt.%), e.g. chromium, nickel, molybdenum and manganese, provides improved properties compared to regular plain carbon steels. Some interesting alloys within this category are the chromium and molybdenum based AISI/SAE 41XX-series. The chromium yields corrosion and oxidation protection while molybdenum enhances strength at high temperatures [9], [27]. The carbon content can vary (0.18-0.61 wt.%), however it is usually kept below 0.2 wt.% to ensure good weldability [10], [27]. Furthermore, these low alloy steels offer a vast range of mechanical properties as they can be tailored through various heat treatments e.g. normalizing, quenching and tempering (see Figure 1), and are significantly cheaper compared to the current ferrous alloys in L-PBF.

For L-PBF limited work has been done on low alloy steels as e.g. 4140 [3], [4], [5] 4130 [6] and 4340 [7], [8]. Yet, with increased knowledge of the L-PBF process, researchers have gained interest of its potential for the automotive industry [4]. Using a build plate temperature of 200°C, Damon et al. [3]. studied process development and the role of intrinsic heat treatment on mechanical properties of 4140. They found that a wide range of process parameters in terms of VED (85-190 J/mm^3), allowed to consistently print cubes up to 99.8% density [3]. In the as-built state the microstructure consisted of small martensitic needles containing precipitates (<100 nm) without a specific orientation. Further, the melt pools could be distinguished by dark boarders which were explained as segregation of carbon [3]. However, no deeper investigation regarding the phases present and their chemical composition was performed. Considering mechanical properties, hardness was found to decrease with the increase of VED. Here, it was suggested that larger VED provides lower cooling rates leading to an increased tempering of the material. In addition, the build rate was improved by using larger scan speeds (11.7 cm^3/h) to the detriment of density (~98%) [3].

In a recent article by Bobel et al. [4], an X-ray imaging technique was used to monitor the in-situ defect evolution during single track experiments as a function of SED (3.0-10.4 J/mm^2) for the 4140 alloy. It was shown that the melt pool depth increases with increased SED and they concluded that the size of the formed martensite had little to no influence of the used energy input. Gas porosities were found within all samples that was identified to be caused by inherent pores in the powder feedstock. However, at the highest SED larger spherical pores explained by the collapse of the bottom of keyholes were observed [4].

The printability of low alloy steels (4130, 4140, 4340 & 8620) has also been investigated at the Powder Metallurgy and Additive Manufacturing group at Chalmers (in the frame of CAM^2) by current PhD student William Hearn and former master student Robert Steinlechner. In their work, different combinations of process parameters (hatch spacing, scan speed, layer thickness and laser power) yielded wide processing windows (90-200 J/mm^3) for densities above 99.8%. They found that the processing window was influenced by the formation of different defects. At low VED, lack-of-fusion occurred due to insufficient melting with the previous layer. On the other hand, at high VED the onset of keyhole formation marked the upper threshold of the processing window. In addition, this work examined the influence of powder bed preheating. It was found that the processability of both 4130 and 4140 alloys increased with increasing preheating temperatures. This was due to reductions in surface cracking. The influence of laser power was examined as well and it was found that the processing windows could be expanded by increasing the laser power. However, this previous work only used a layer thickness of 20 μm meaning the fastest build rate, that could achieve the desired density, was only 6.8 cm^3/h.

To conclude, limited research has been conducted on low alloy steels for L-PBF. However, the large processing windows obtained in previous studies shows great potential. As previously described, low build rate is a bottleneck for broader application of L-PBF components. Therefore, this thesis intends to improve the build rate of low alloy steels by increasing the layer thickness and further investigate how changes in layer thickness affect the development of defects. This will provide additional knowledge to a still novel material for L-PBF.

3. Method

3.1 Powder feedstock

In Table 1, chemical compositions of the pre-alloyed, gas-atomized low alloy steel powders used in this project are presented. The alloys are similar in composition with an exception of a 0.13 wt.% higher carbon content in the 4140. The powders had a particle size distribution 20-53 µm as defined by the powder provider.

Table 1. Chemical composition of 4130 and 4140 as described by the manufacturer.

ALLOY	**C**	**Cr**	**Mo**	**Mn**	**Si**	**P_{max}**	**S_{max}**
AISI 4130	0.34	1.0	0.2	0.6	0.3	0.01	0.006
AISI 4140	0.47	1.0	0.2	0.6	0.2	0.011	0.007

3.2 L-PBF processing

Printing was done on an EOS Gmbh M290 machine that is equipped with an ytterbium fiber laser with the beam diameter of 100 µm. Further, the prints were performed with a 180°C preheating of the build plate and a constant flow of Ar kept an inert atmosphere where the oxygen content was held below 0.1%. For more technical specifications of the machine, see Table 2.

Table 2. Technical specifications of EOS Gmbh M290 as defined by manufacturer

EOS M 290	
Build volume	250 mm x 250 mm x 325 mm
Laser source	400 W Yb-fiber
Scan speed	Max 7000 mm/s
Beam diameter	100 µm
Preheat of build plate	0-200 °C

3.3 Selection of process parameters

3.3.1 Evaluation of VED & SED as design parameters when varying the layer thickness

A preliminary set of experiments were performed in order to understand the optimal choice of process parameters when varying the layer thickness. The process parameters used can be found in Table 3. The laser power, scan speed, hatch spacing and layer thickness were varied with the main interest to investigate how density changed with VED and layer thickness.

Table 3. Process parameters of preliminary design of experiments.

Sample	Laser Power (W)	Scan Speed (mm/s)	Hatch Spacing (µm)	Layer Thickness (µm)	VED (J/mm^3)
1	195	880	90	20	123
2	195	1320	90	20	82
3	195	1100	90	20	98
4	156	880	90	20	98
5	156	1320	90	20	66
6	234	880	90	20	148
7	156	1100	90	20	79
8	234	1320	90	20	98
9	234	1100	90	20	118
10	214	928	100	40	58
11	257	928	100	40	69
12	171	742	100	40	58
13	171	928	100	40	46
14	214	1114	100	40	48
15	171	1114	100	40	38
16	214	742	100	40	72
17	257	1114	100	40	58
18	257	742	100	40	87
19	184	600	120	60	43
20	230	600	120	60	53
21	276	600	120	60	64
22	184	750	120	60	34
23	230	750	120	60	43
24	276	750	120	60	51
25	184	900	120	60	28
26	230	900	120	60	35
27	276	900	120	60	43

In Figure 4, the influence of VED on relative part density is illustrated for the 4130 and 4140 alloys at layer thicknesses of 20, 40 and 60 µm. The VED range where high density specimens (>99.8%) are achieved, narrows as the layer thickness is increased.

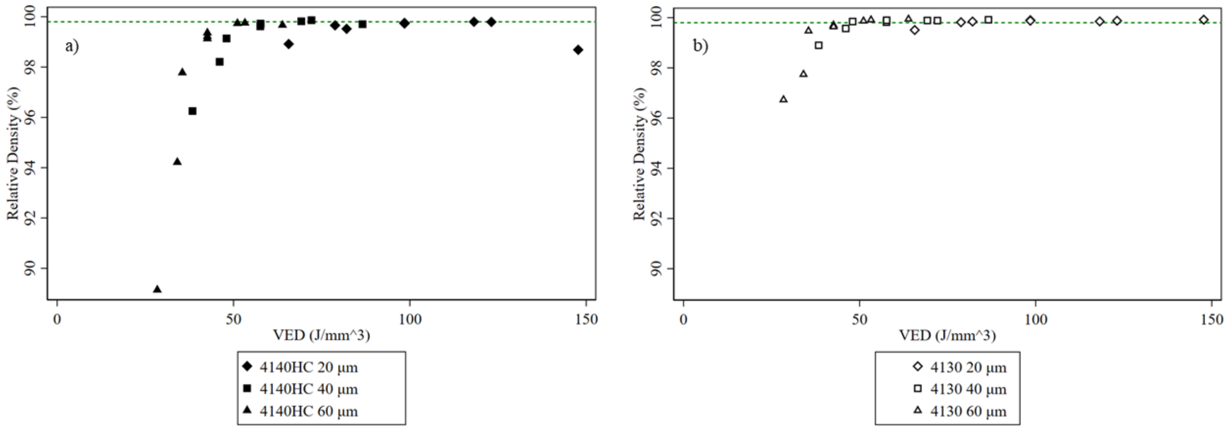

Figure 4. Influence of VED on relative density at varied layer thickness for 4140 a) and 4130 b).

Even though trends are present in Figure 4, altering a wide variety of process parameters (e.g. layer thickness and hatch spacing), impose significant scaling by using VED as a combined process parameter. For example, in order to achieve the same VED at 20, 40 and 60 µm layer thickness, assuming a constant laser power and hatch spacing, the scan speed would have to decrease by ~50-66% with respect to the 20 µm layer thickness. This will consequently affect the melt pool characteristics at the different layer thicknesses (see Section 2.2.4). Due to the inability to decouple the VED from the layer thickness another design parameter was examined, the surface energy density SED. Compared to VED, the SED is independent of the layer thickness and is a function of only the laser power (P), scan speed (v) and hatch spacing (h).

$$SED = \frac{\mathrm{P}}{\mathrm{v} * \mathrm{h}} \quad [\mathrm{J/mm^2}]$$

In Figure 5, the same density values are presented as a function of SED (J/mm^2). Here, a clearer trend is revealed where the processing window changes location to higher SED as layer thickness increases. This suggests that SED could be a beneficial parameter to use when varying the layer thickness.

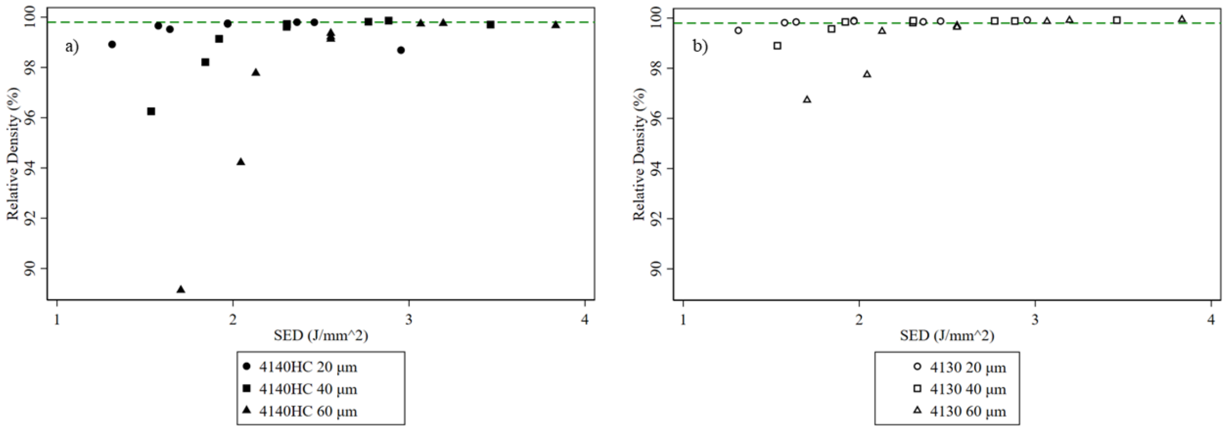

Figure 5. Influence of SED on relative density at three different layer thicknesses for 4140 a) and 4130 b).

By illustrating the density versus SED for each layer thicknesses separately, see Figure 6 a) and b), interesting regions in process space are revealed. In Figure 6 a), a potential processing window between 1.9-3.5 J/mm^2 is observed at a layer thickness of 40 µm. While the printable region for a 60 µm layer thickness was found to be at slightly higher SEDs between 2.5-3.8 J/mm^2.

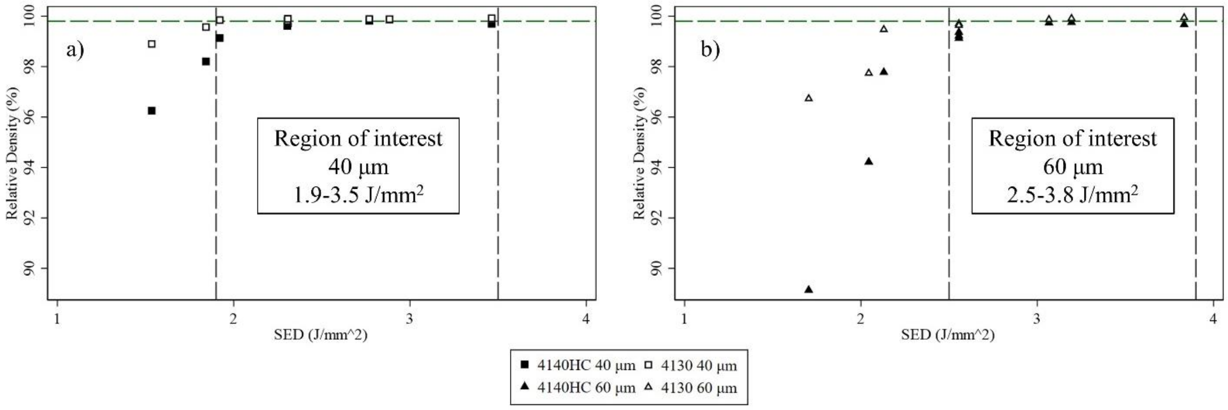

Figure 6. Possible processing windows for 4140 and 4130 alloys, defined in ranges of SED (J/mm^2) at 40 µm a) and 60 µm b).

By considering these results it was decided that the main experiment would be designed based on ranges of SED. 24 samples were printed at each layer thickness (40 & 60 µm) using 170 W, 210 W and 250 W laser power for both alloys. The process region investigated was between 2.4 and 3.8 SED J/mm^2 based on the regions of interest in Figure 6. In order to limit the amount of varied process parameters the hatch spacing was kept constant and the SED range was obtained by mainly varying the scan speed.

3.4 Metallography

In order to analyze the printed samples, the following steps were performed:

1) Sectioning of samples using an Isomet 2000 precision saw by Buehler, yielding vertical cross sections parallel to the build direction (z-x axis), see Figure 7.
2) Mounting in PolyFast resin by using the Struers CitoPress-20.
3) Grinding via SiC-foil and by successively increasing grit size in the following order #220, #320, #500, #800, #1200, #2000, #4000 for 1 min at each grit size.
4) Polishing applying 3 and 1 µm suspension for 15 minutes respectively.
5) Etching using 3% Nital solution.

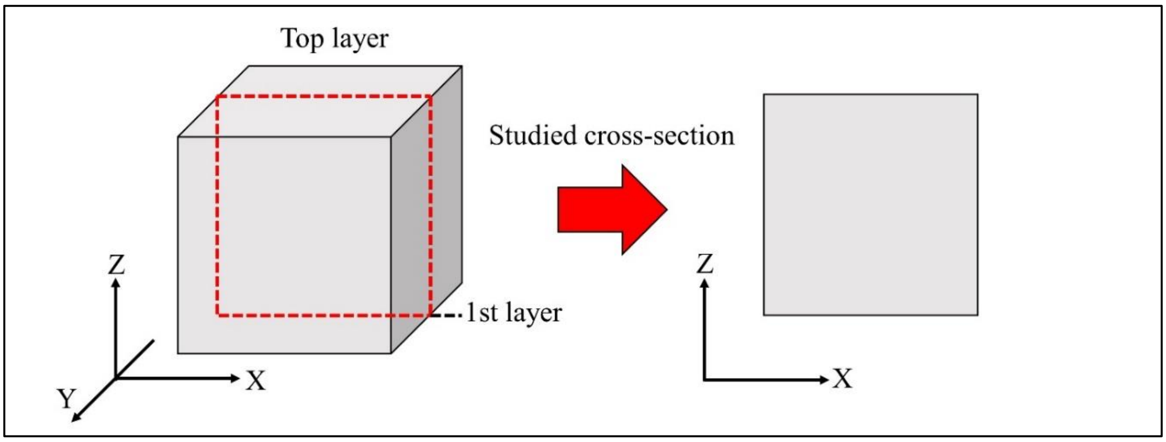

Figure 7. Schematic of the sectioning performed on each sample. All analysis steps were performed on the same cross section.

3.5 Light optical microscope

Images of microstructural features were obtained by a Zeiss Axioscope 7 light optical microscope (LOM). The ZenCore software was utilized to obtain stitched micrographs for density analysis.

3.6 Scanning electron microscope

A Leo Gemini 1550 scanning electron microscope (SEM) was used to obtain high resolution micrographs of the microstructure.

3.7 Density measurements

Density of the samples was calculated using FIJI image analysis software and followed a specific workflow, illustrated in Figure 8. Stitched images (Figure 8 a) were cropped to exclude the surrounding mounting resin to solely capture the bulk material (Figure 8 b). These images were made binary for the software to calculate the area percentage of defects present, distinguishing bulk material from defects by applying an intensity threshold. As shown in (Figure 8 c) the threshold yields a contrast in coloration where the bulk material is white and defects black.

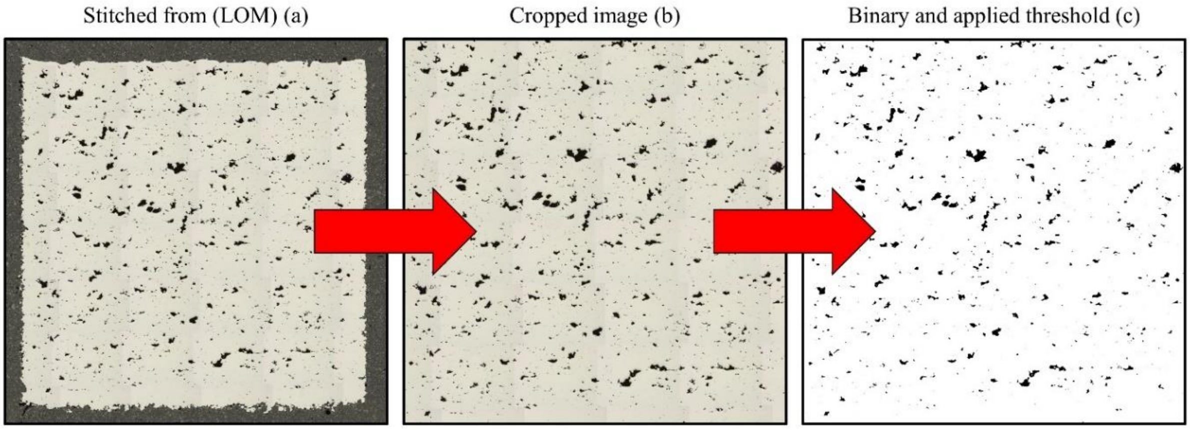

Figure 8. Workflow schematic of bulk density measurements.

3.8 Hardness measurements

Bulk hardness was measured according to ASTM standards on a Struers DuraScan, see Figure 9 a). Indentations (HV10) were performed in a 4x4 with a 2.5 mm distance between. Four cross sections were tested per run. An example of typical gained indentations is depicted in Figure 9 b).

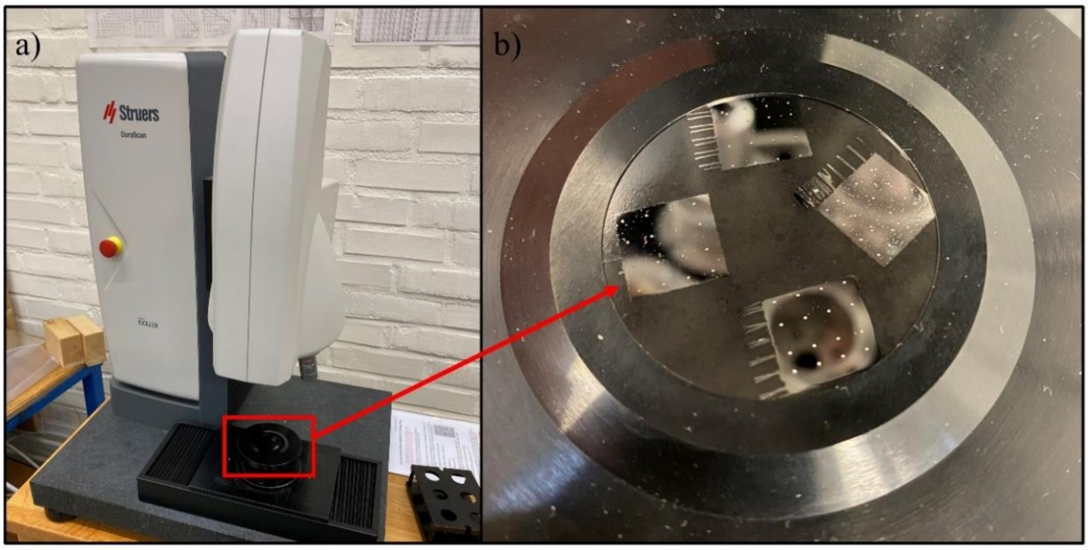

Figure 9. DuraScan hardness tester with mounted samples a) and a higher magnification image of the 16 indentations performed on each sample cross section b).

3.9 Melt pool characterization

In order to calculate melt pool depth, light optical micrographs were taken of etched sample cross-sections and subsequently measured in the FIJI software. In Figure 10, an example of a melt pool depth measurement is presented. The melt pool is indicated by the red ellipse and the depth estimated by the distance of the black arrow. For each sample ~ 30 measurements were made across the top layer for the melt pool depth.

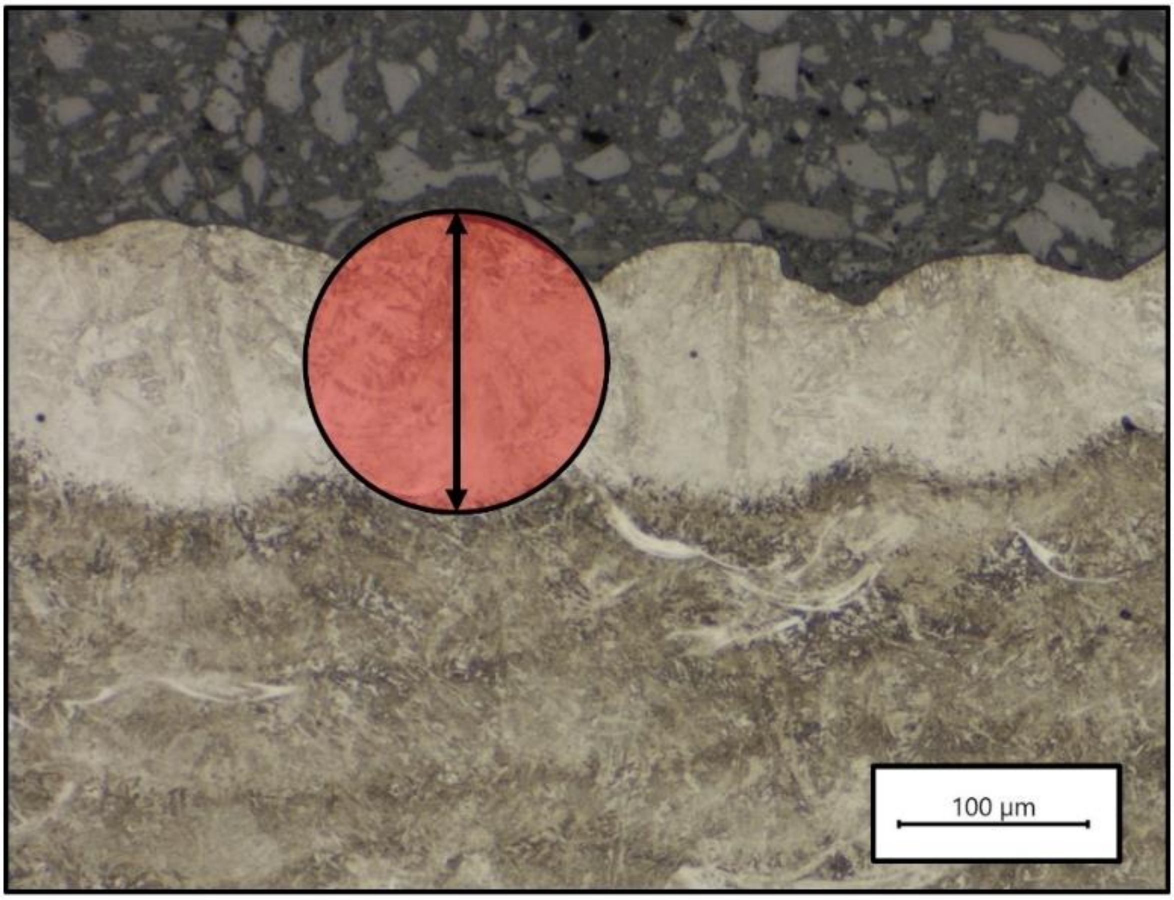

Figure 10. Illustration of the methodology used for melt pool depth measurements where the depth is indicated by the black arrow within the red ellipse.

4. Results

4.1 Defects

In this section a description of the various types of defects that were found in the produced specimens will be outlined.

4.1.1 Porosities

The first type of porosity found was characterized by its sharp and irregular shape, leaving traces of un-melted regions in the microstructure, see Figure 11 a-c. As described in literature, these are typical traits of lack-of-fusion porosities, commonly observed when the energy volume is too low to ensure bonding between subsequent layers or adjacent melt tracks [19]. At 50x magnification, illustrated in Figure 11 a), lack-of-fusion porosities can be seen in a measured size range of 70-500 μm. In Figure 11 b), 200x magnification revealed un-melted powder particles located inside the irregular pores. At even higher magnification, SEM micrographs indicated large voids between the bottom of melt pools and the previously deposited layer. These voids were in some regions larger than the layer thickness (75-110 μm), see Figure 11 c) for t=60 μm at SED=2.4 J/mm^2.

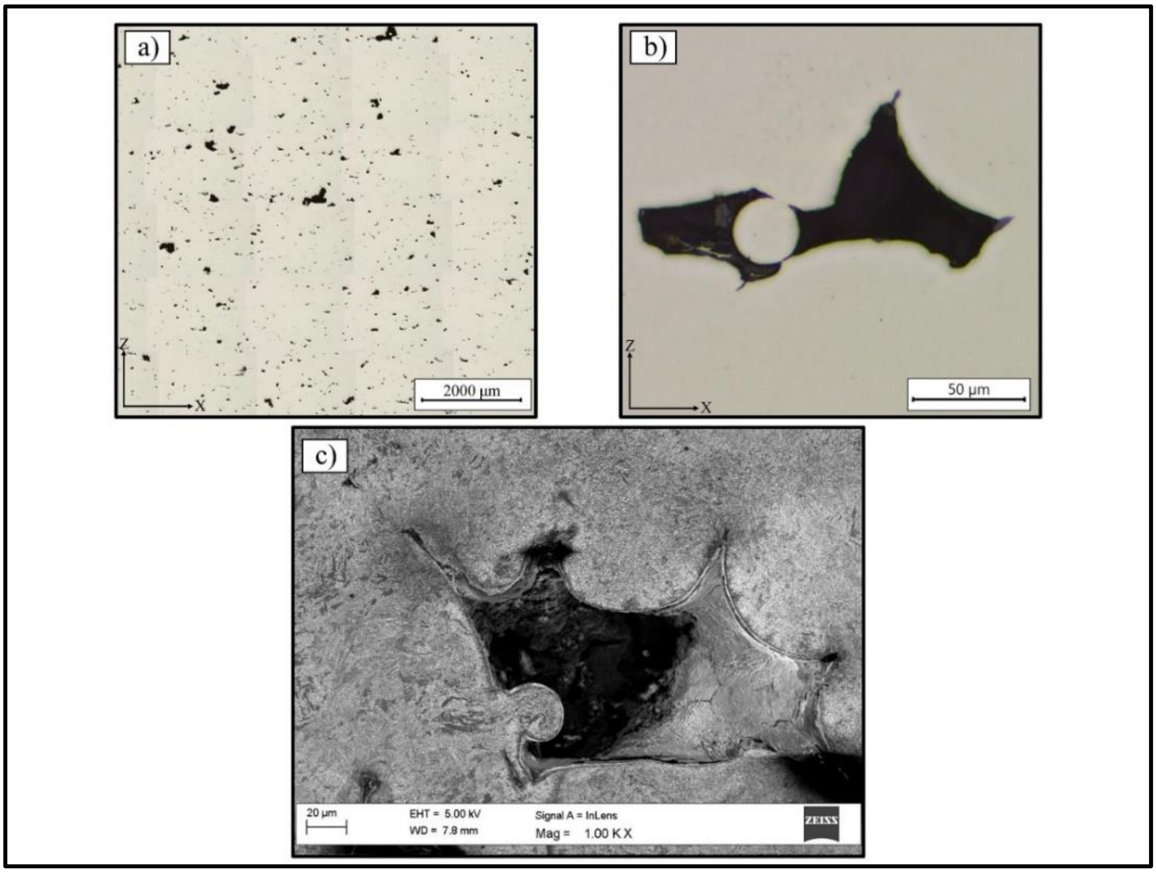

Figure 11. Characteristic lack-of-fusion porosities found in this study presented at 50x magnification (LOM) a). At higher magnification of 200x the typical traits of unmelted powder were found in the interior of the unmelted regions (LOM) b). Higher resolution SEM micrographs revealed ~75-110 μm gaps between the bottom of melt pool and the previous layer at low SED and 60 μm layer thickness.

A third sort of pore was identified within all investigated samples, distinguished by its small size and spherical shape. An example is depicted in Figure 12 at 200x magnification, where pores of 0.5-10 µm can be seen randomly distributed across the sample cross-section marked by red arrows.

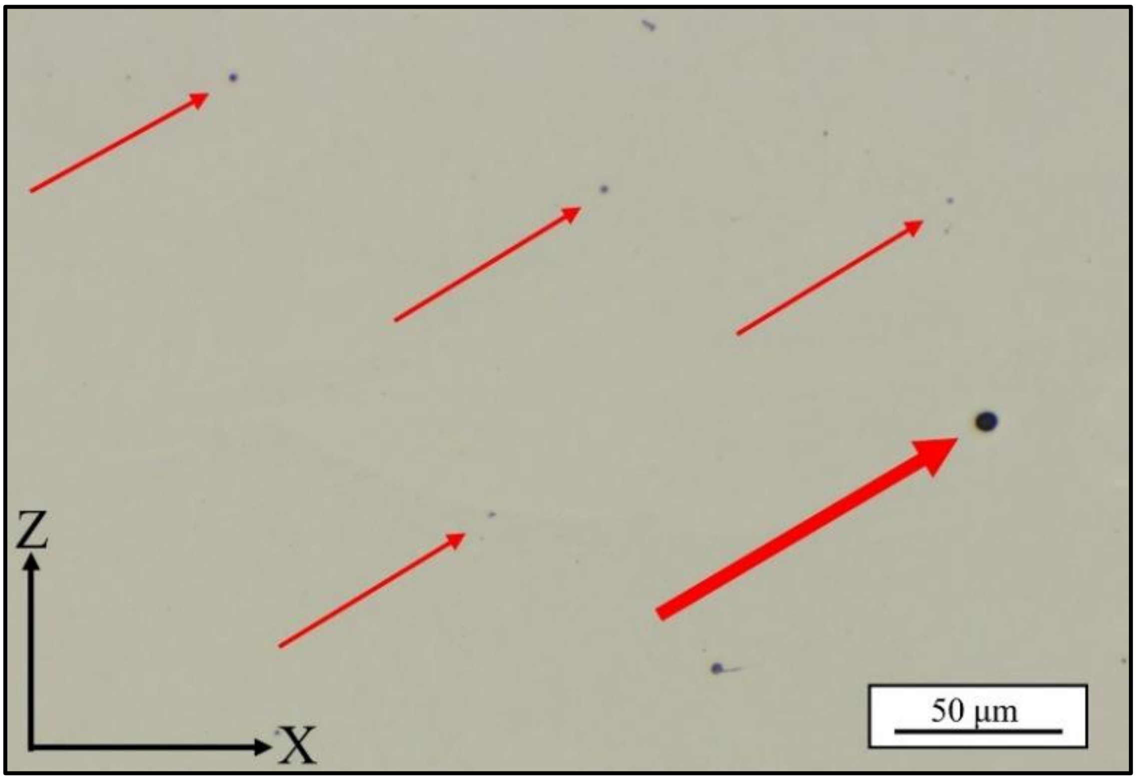

Figure 12. Illustration of fine spherical pores (0.5-10 µm in diameter) that were found within all investigated samples

4.1.2 Cracks

Another category of defects that were observed were cracking defects. Two types of cracks were found within the produced specimens and were only found when processing the 4140 alloy.

In Figure 13, a light optical micrograph of an etched 4140 cross section illustrates a crack originating from a notch at the sample surface propagating perpendicular to the build direction. These cracks were in the order of 70-130 µm and found for both tested layer thicknesses when using a low surface energy density (below 3.0 J/mm^2). The combination of high carbon content (0.47 wt.%), yielding a large carbon equivalent, and increased cooling rates at lower SED are suggested to be a potential cause for this type of cracking.

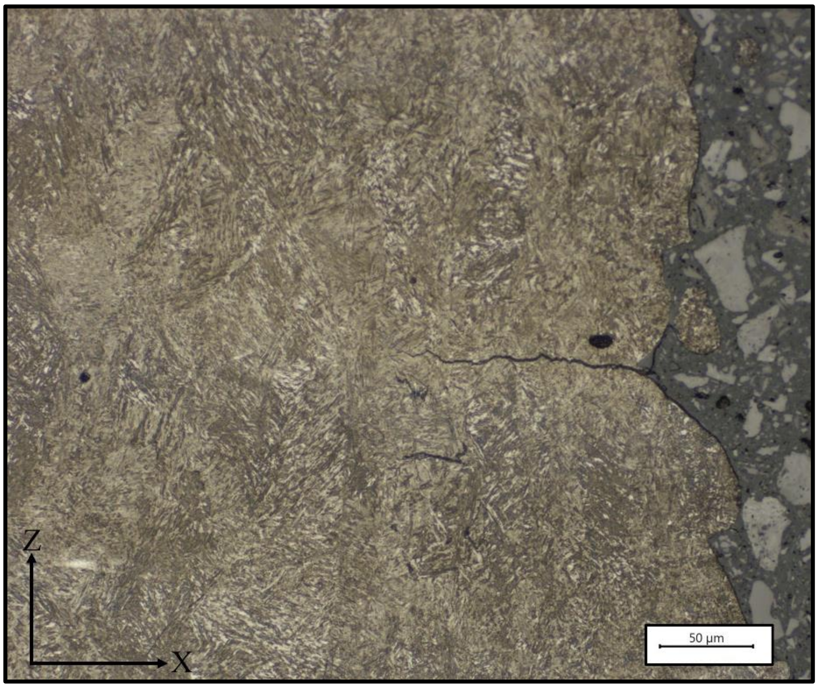

Figure 13. Surface crack propagating perpendicular to the build direction in a cross-section of 4140 steel.

Characterized by its small size (10-100 µm) and stretching in the build direction, the last type of crack was found to be randomly distributed within all 4140 specimens, see Figure 14. 3% Nital solution revealed that these cracks seamed to form along grain boundaries. This can be visualized at different magnifications in Figure 15 (a) (LOM micrograph) and Figure 15 (c-d) (SEM micrographs) where the cracks are highlighted with yellow arrows.

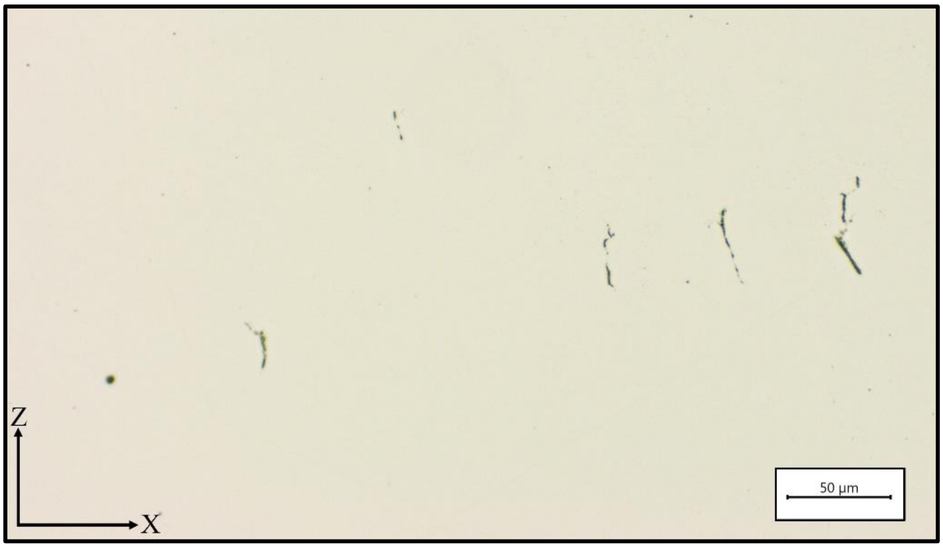

Figure 14. Illustration of typical small cracks found within all 4140 samples.

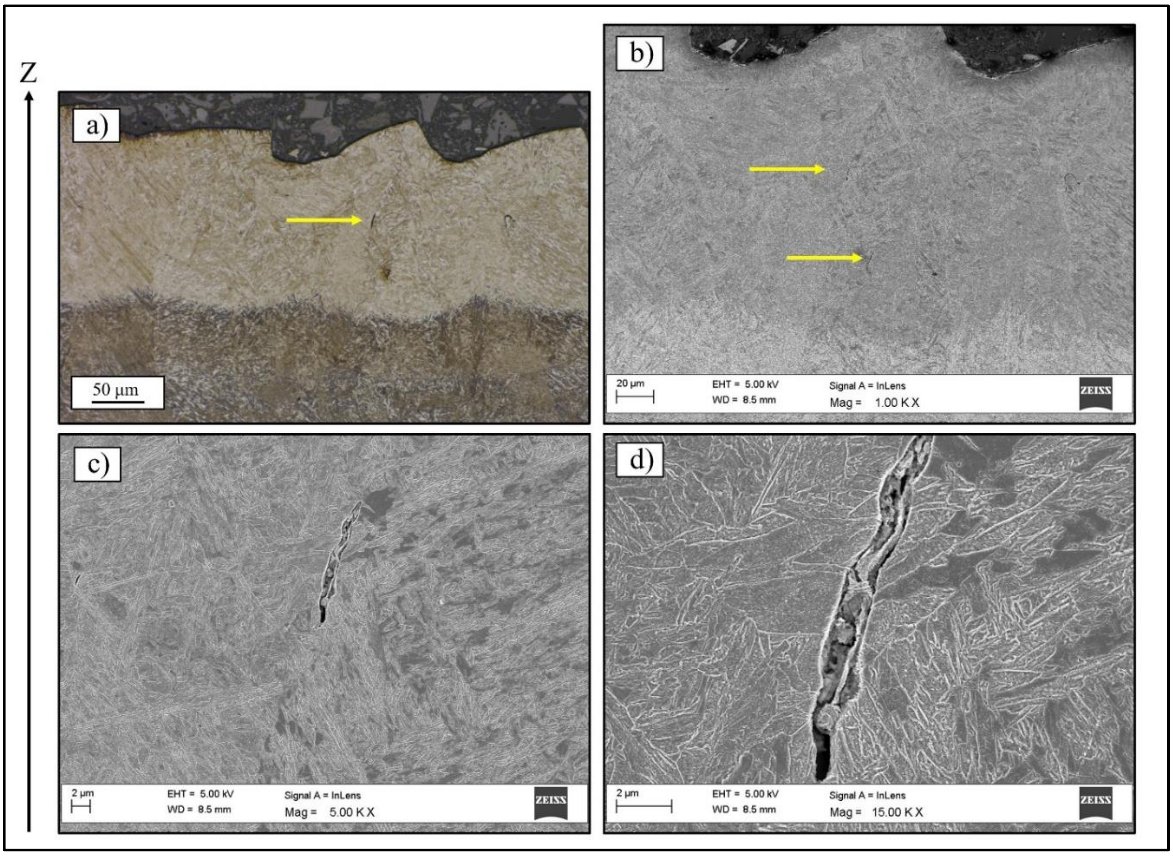

Figure 15 Illustration of typical cracks found within 4140 samples indicated by the yellow arrows (LOM a)) and (SEM micrographs a-d). The cracks seams to follow boarders of distinct microstructural features.

4.2 Processing Windows

In the following section processing windows are illustrated for both the 4130 and 4140 alloys, produced at layer thicknesses of 40 and 60 µm. The printable region is defined by SED values where part density was measured at greater than or equal to 99.8 %. For visual aid, horizontal green lines are inserted into the plots to mark the approved density threshold. In addition, micrographs of sample cross sections, inside and outside the processing window, are presented to compare the defects present.

4.2.1 4130: 40 µm layer thickness

In Figure 16, the processing window for 4130, produced at a layer thickness of 40 µm, is illustrated. Here densities over 99.8% were achieved across a wide SED range yielding a processing window of 2.6-3.8 J/mm^2. At a layer thickness of 40 µm, changes in the laser power do not noticeably affect the optimal SED processing window. The influence of SED can be seen, as density slightly increase at larger SED. Looking at Figure 17 a), irregular pores are present, indicating lack-of-fusion, as well as small spherical pores that are distributed over the entire sample. At a larger SED of 3.6 J/mm^2, see Figure 17 b), no lack-of-fusion is observed, with only a few spherical pores being present.

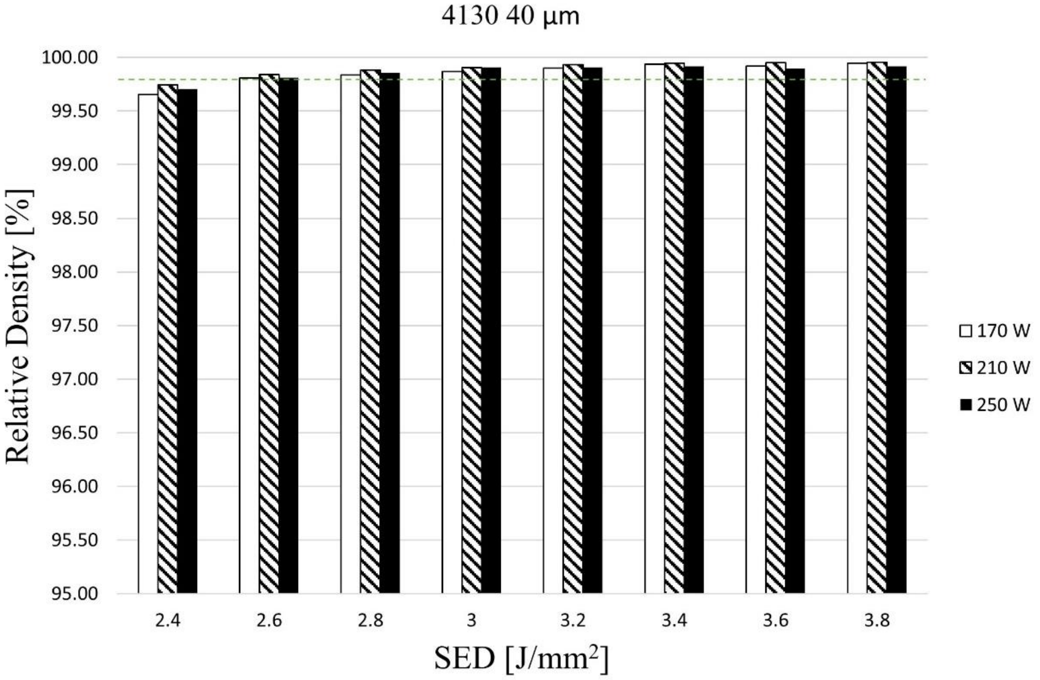

Figure 16. The influence of surface energy density on part density of the 4130-alloy at 170 W, 210 W and 250 W using a 40 µm layer thickness.

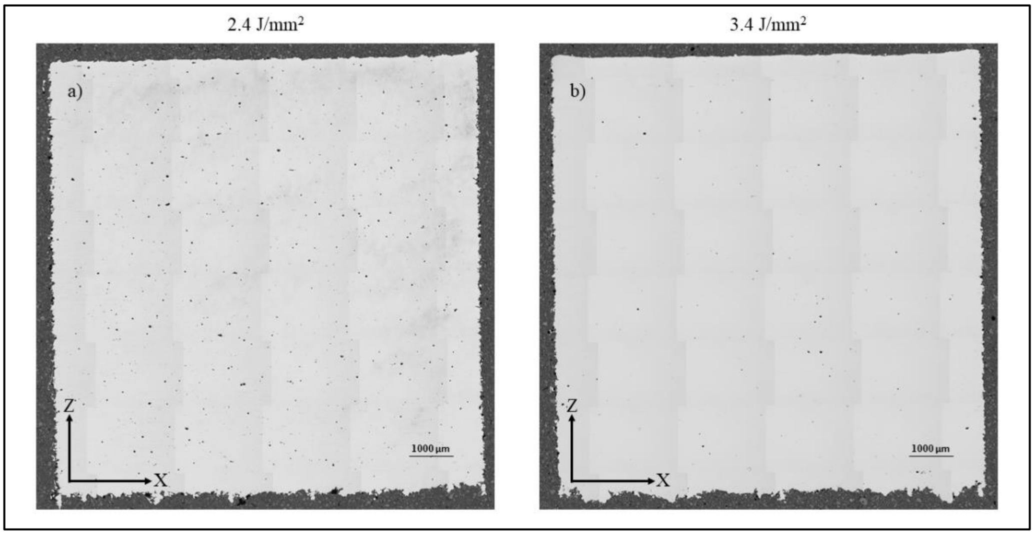

Figure 17. Micrographs of 4130 cross sections illustrating differences in porosity at 2.4 J/mm² a) and 3.4 J/mm² b).

4.2.2 4130: 60 µm layer thickness

By increasing the layer thickness to 60 µm, the processing window is shifted towards larger SED values (3-3.8 J/mm^2) and is narrower compared to the 40 µm, as shown in Figure 18. A greater influence of laser power on part density can be observed, especially at low SED, as higher densities were gained when using the highest laser power of 250 W. This indicates that increased laser power shifts the printable region to lower SED and is more important at a larger layer thickness. It should be noticed that the 170 W laser power failed to yield approved density in the investigated SED range.

Similar to the 40 µm samples, lack-of-fusion is present at low SED. A typical example of a lack-of-fusion dominated cross section is presented in Figure 19 a). Compared to the 40 µm layer thickness, at equivalent parameters, significantly larger defects are present. This points that an increased layer thickness pushes the printable region to higher SEDs. As for the lower layer thickness, once the energy delivered to the powder is enough, no lack-of-fusion occurs, and required densities are achieved, see Figure 19 b).

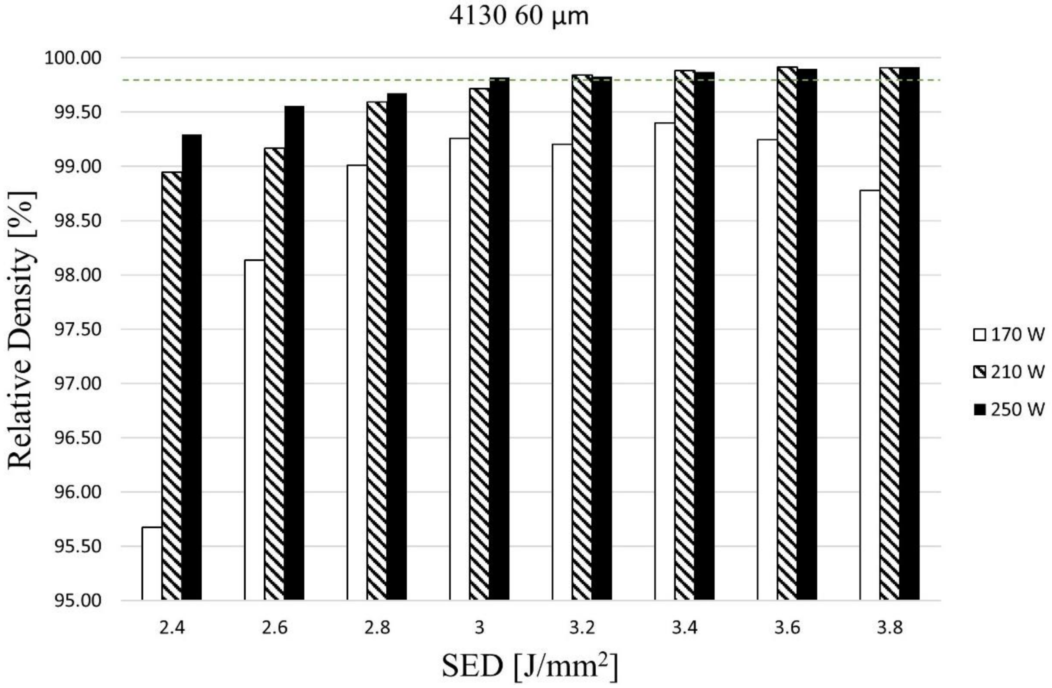

Figure 18. The influence of surface energy density on part density of the 4130-alloy at 170 W, 210 W and 250 W using 60 µm layer thickness.

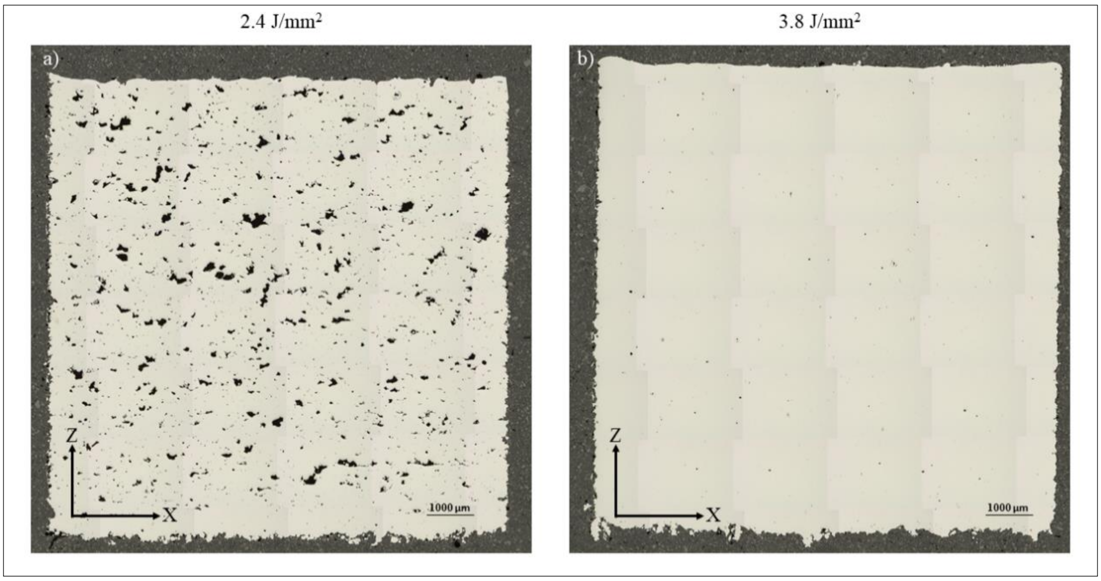

Figure 19. Unetched micrographs of 4130 cross sections illustrating differences in porosity at 2.4 J/mm² (170 W) a) and 3.8 J/mm² (250 W) b).

4.2.3 4140: 40 μm layer thickness

At 40 μm layer thickness, seen in Figure 20, a processing window between 2.8 and 3.6 J/mm^2 was established for the 4140 alloy. Again, sample density is observed to increase at elevated SED. However, in contrast to the 4130 samples, fluctuations in density could be distinguished. Densities passed 99.8% were only gained for the two larger laser powers and no noticeable differences were seen between them. In addition, cubes printed at 170 W did not result in approved densities. Overall, the sample densities of the 4140 alloy were lower than that of the 4130 alloy. A possible reason could be the presence of the small cracks that were described in Section 2.3.5.

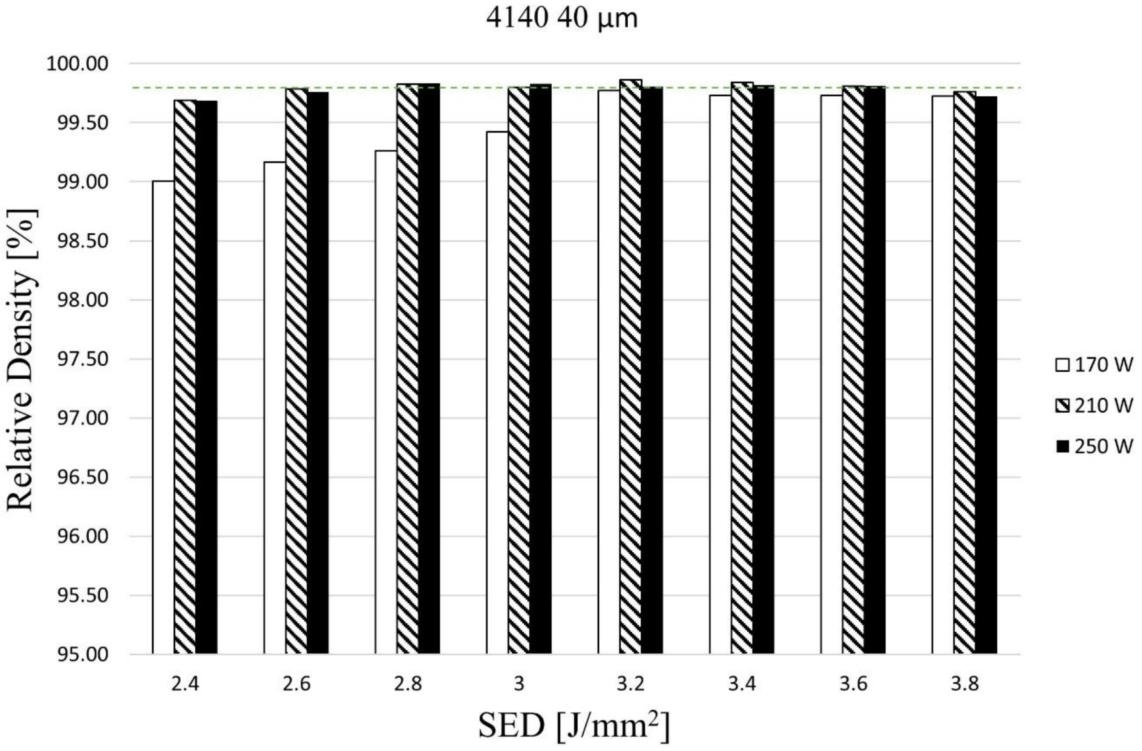

Figure 20. Influence of surface energy density on part density of the 4140-alloy at different laser powers 170 W, 210 W and 250 W using 40 μm layer thickness.

4.2.4 4140: 60 μm layer thickness

The processing window obtained for the 4140 alloy, at a layer thickness of 60 μm, is illustrated in Figure 21. Between 3.4-3.6 J/mm^2, approved densities where achieved. Equivalent to the 4130 alloy, moving from a 40 to a 60 μm layer thickness yields lower density at low SED, which is especially pronounced at 170 W laser power. It can be observed that the density becomes less predictable when increasing layer thickness.

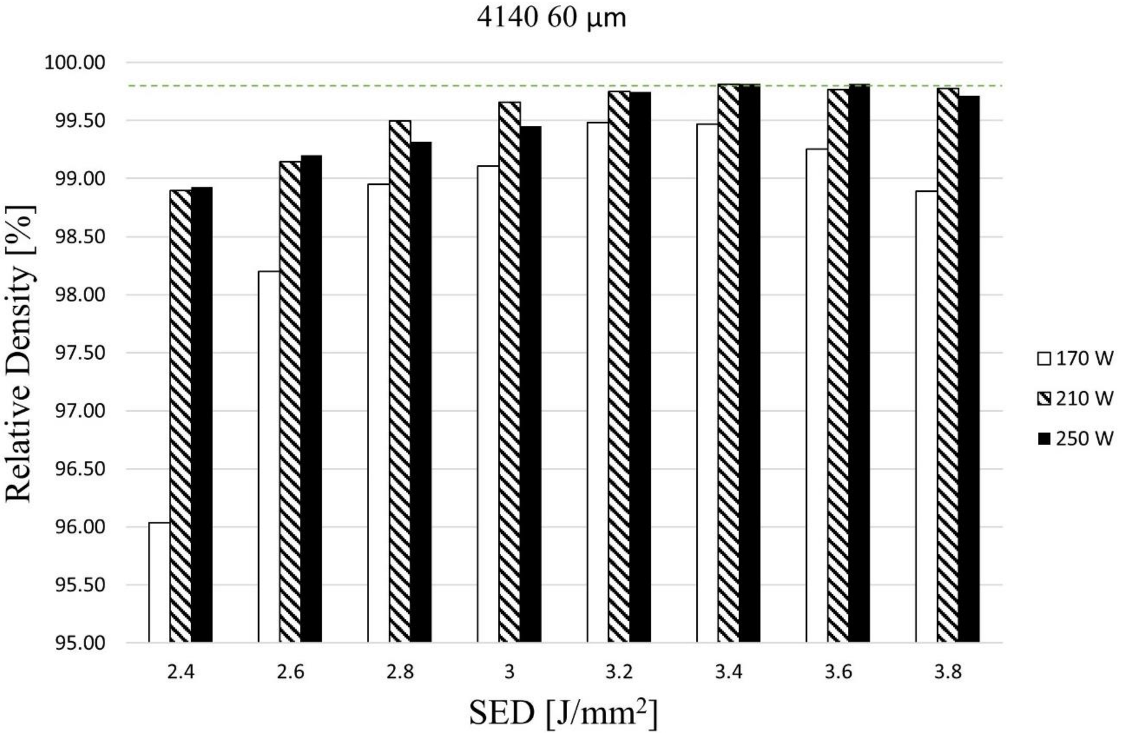

Figure 21. The influence of surface energy density on part density of the 4140-alloy at 170 W, 210 W and 250 W using 60 µm layer thickness.

4.3 Melt pool characteristics

4.3.1 Melt pool depth in case of 4130 steel

In Figure 22 the melt pool depth as a function of SED is illustrated. For all operated laser powers at 40 µm, it is observed that the depth increases (99-220 µm) in an approximately linear fashion with SED. This trend can be explained by a higher energy input as SED increases, allowing for more melting of the material. In addition, an effect of the laser power is seen where deeper melt pools are yielded when operating at a higher laser power.

The 60 µm layer thickness shows a comparable trend with the 40 µm as the melt pool becomes deeper (116-224 µm) with increased SED and higher laser power. No major differences were observed regarding the influence of layer thickness and the gained melt pool depth as comparable depths were measured at the same SED and laser power. This indicates that when examining the SED, changes in the layer thickness do not have a noticeable effect on the depth of the melt pool.

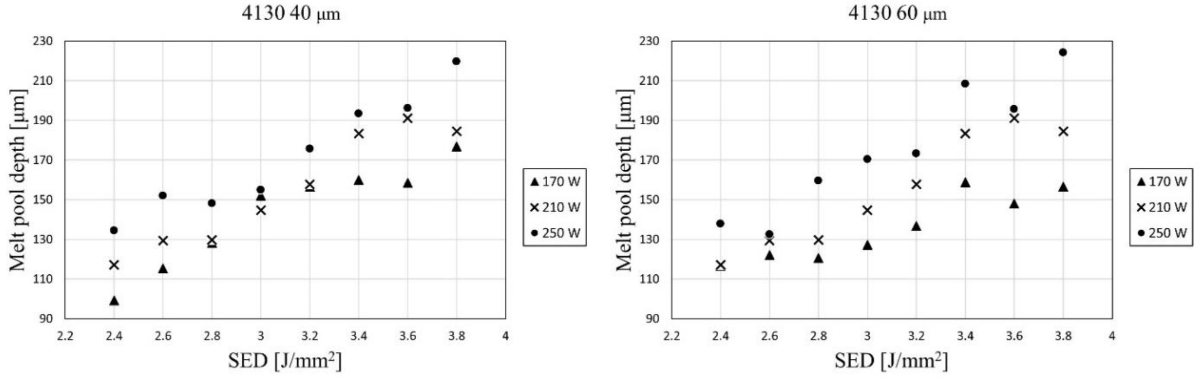

Figure 22. Influence of SED and laser power (W) on melt pool depth (µm) for 4130, using 40 µm layer thickness.

In Figure 23, etched cross sections used for melt pool measurements of the top layers are presented. At low SED the melt pool is small with an average melt pool depth of 117 µm and is easily distinguished by its semicircular shape due to less overlap with adjacent melt tracks, see Figure 23 a). A 0.2 J/mm^2 increase in SED yielded 130 µm melt pool depth and the melt pool boundaries are less visible due to greater overlap between adjacent melt pools. As the SED increases further the depth is increased to 171 µm and by looking at Figure 23 c), the overlap is so large that it is difficult to visualize melt pool boundaries. Thus, the size and shape of the melt pool is altered by increasing the SED, resulting in increased melt pool depth and width.

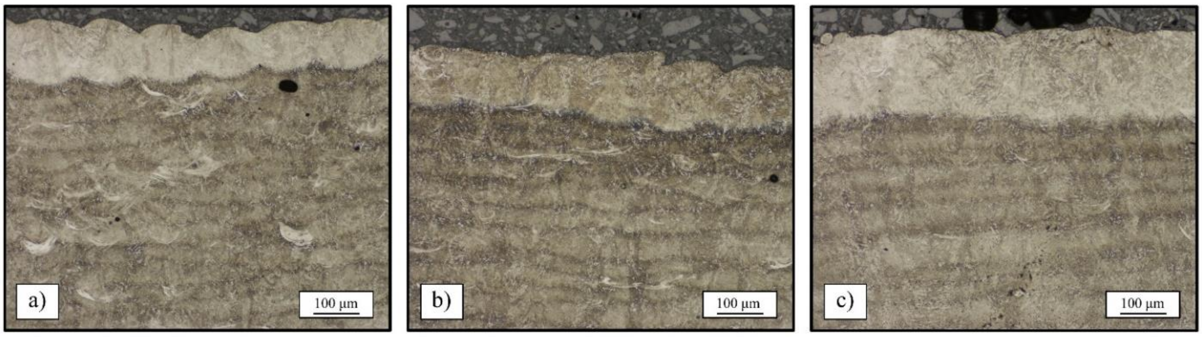

Figure 23. Melt pool evolution with increased SED at 2.4 a), 2.6 b) and 3.6 J/mm² c) for the 40 µm layer thickness.

4.3.2 Melt pool depth in case of 4140 steel

The results of the 4140 melt pool depth measurements are illustrated in Figure 24. As with the 4130 alloy, there is an approximately linear relationship between obtained depth and energy delivered to the material. Here, deeper melt pools were gained by using a larger laser power when SED was kept constant at both thicknesses. It was investigated whether layer thickness had an influence on melt pool depth and as for the 4130 alloy no clear trend could be seen across all laser powers.

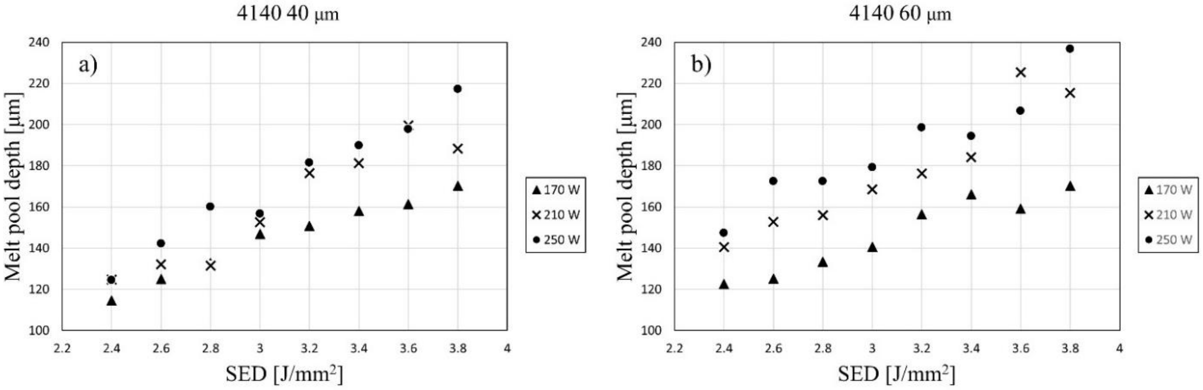

Figure 24. Influence of SED and laser power (W) on melt pool depth (µm) for 4140, using 40 µm layer thickness a) and 60 µm b).

4.4 Microstructure

A LOM micrograph of an etched (3% Nital) cross section revealed distinct contrast in microstructure of the last deposited layer compared to the underlying layers, see Figure 25 a). In Figure 25 b), high magnification SEM images showed that martensitic laths are present with no noticeable difference in morphology and size at the magnifications studied. A potential fusion line is marked by the yellow arrows and the morphology of the laths seems to stretch perpendicular to this fusion line. This microstructure was representative for all investigated samples and no apparent alterations between used parameters and microstructure could be observed at high magnification.

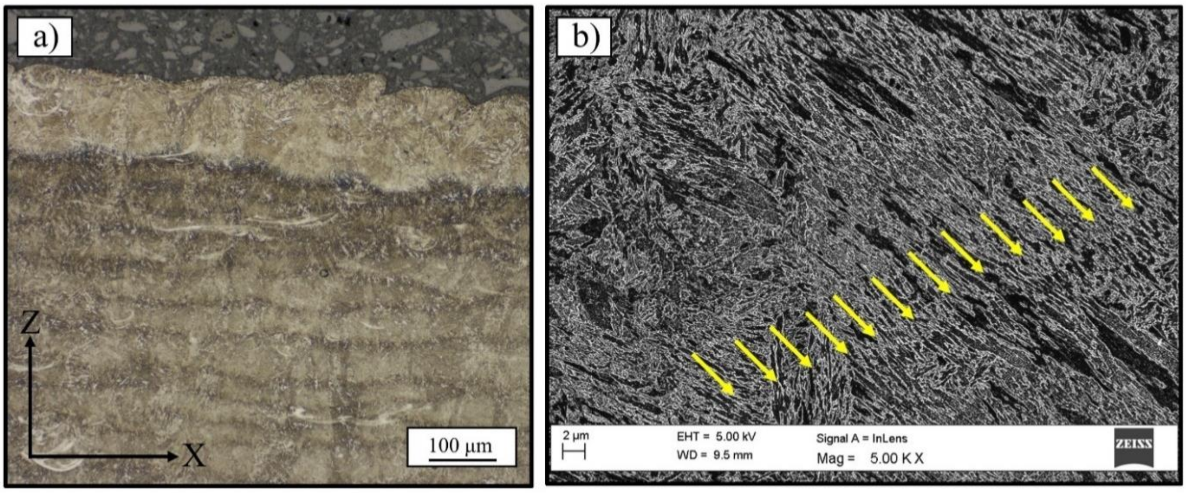

Figure 25. General microstructure of 4130 cross section etched by 3% Nital (LOM) a) and (SEM) b). The light optical micrograph a) shows bright regions with little reaction to the etchant typical of martensitic structure and the darker regions indicate a tempered zone. SEM images at 5000x magnifications b) indicates a tempered martensitic lath structure with a possible fusion line (indicated by the yellow arrows). Note that no clear differences in size and morphology of the tempered martensite was observed at high magnification.

4.5 Hardness

In the following section, hardness values are presented as a function of VED instead of SED. As the hardness have been shown to correlate to the volume of remelted/reheated material instead of just a specific 2D area [3].

4.5.1 Hardness of 4130 steel

Obtained hardness values (HV10) are shown in Figure 26 at a 40 µm layer thickness as a function of VED and laser power. A linear decline in hardness was seen from low to high VED (~405-360 HV10), which correlates to an increased size and depth of the melt pool as the VED increases. A larger melt pool increases the heat input and hence exposure time for the re-melted material that will induce more tempering of the material. In addition, it was found that a higher laser power of 250 W yielded lower hardness compared to 210 W and 170 W. It is suggested that this trend is related to the deeper penetration gained using higher laser power as shown in Figure 22. A deeper melt pool at an increased laser power can induce higher heat exposer of previously built layers, leading to greater reheating and an increased amount of tempering during processing.

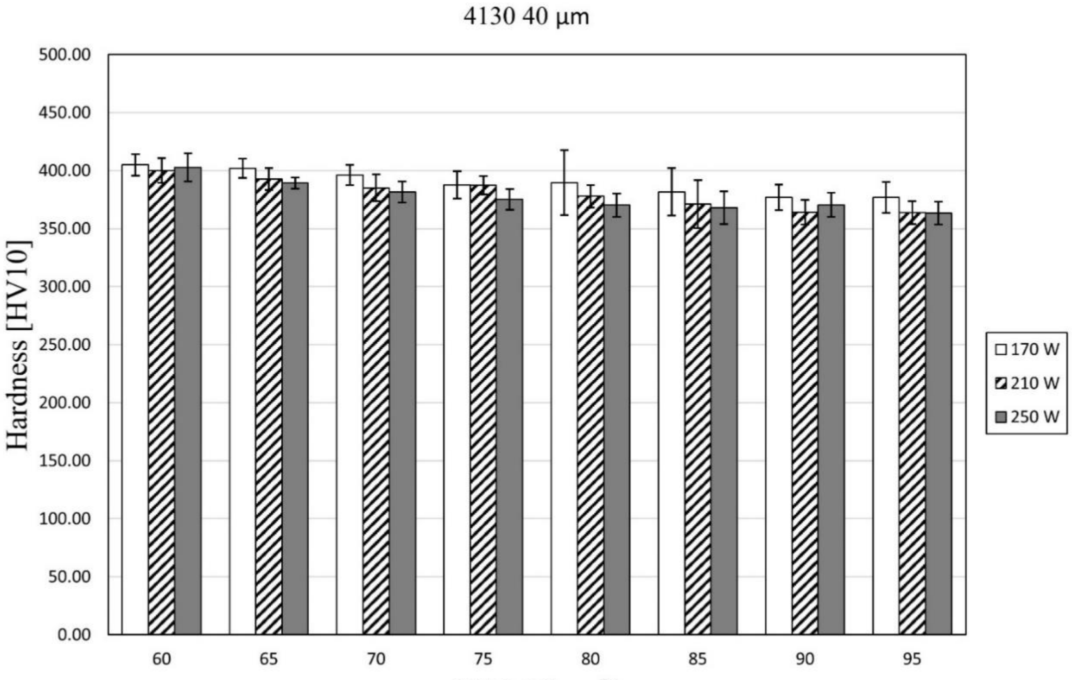

Figure 26. Illustration of the hardness (HV10) evolution with increased VED (J/mm³) and the influence of laser power using 170 (W), 210 (W) and 250 (W) for the 4130 alloy and 40 (µm) layer thickness.

In Figure 27, the hardness for the 4130 alloy produced with 60 µm layer thickness is represented. By increasing the layer thickness, an initial increase in hardness is observed at low VED (~370-400

HV10). This early increase in hardness is explained by the high porosity found at these low VED values. In Figure 28 a), large lack-of-fusion pores are present which explains the lower hardness and the large standard deviations (±47 HV10) that can be seen at low SED. Examining Figure 28 b), no defects are visible close to the indention and the smaller standard deviation (±15 HV10). Following the initial increase in hardness a general decline with increased VED was observed (~400-360 HV10) at approximately 46.7 J/mm^3.

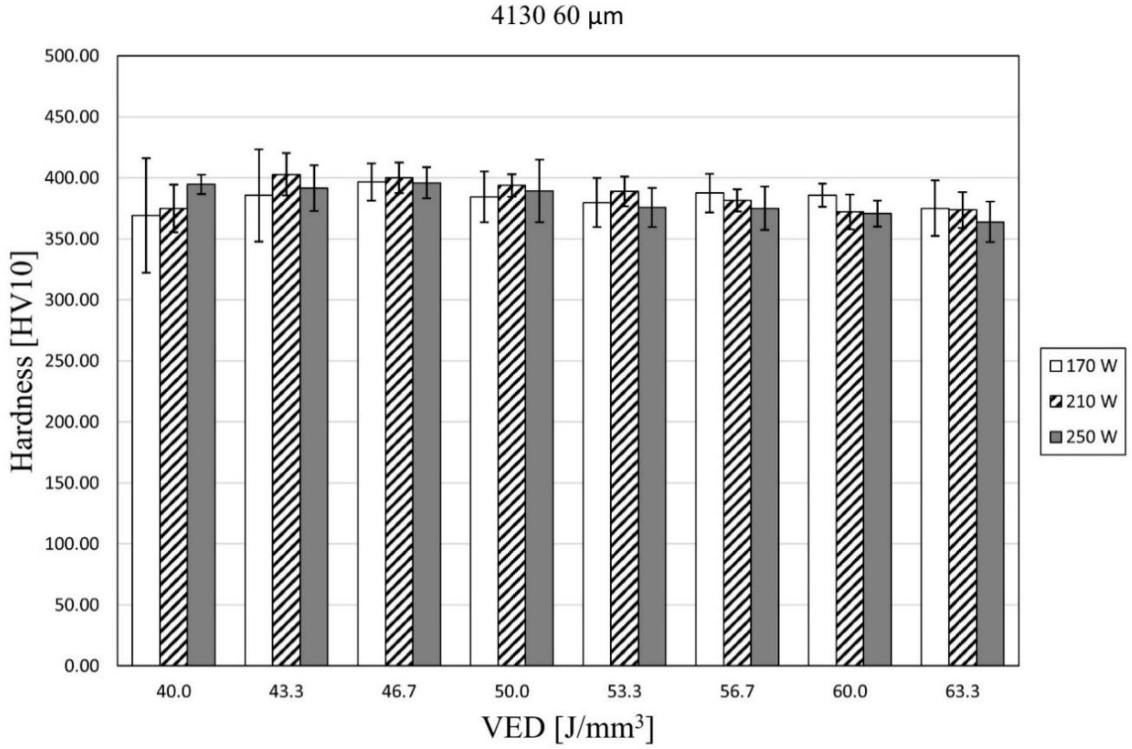

Figure 27. Illustration of the hardness (HV10) evolution with increased VED (J/mm³) and the influence of laser power using 170 (W), 210 (W) and 250 (W) for the 4130 alloy and 60 (µm) layer thickness.

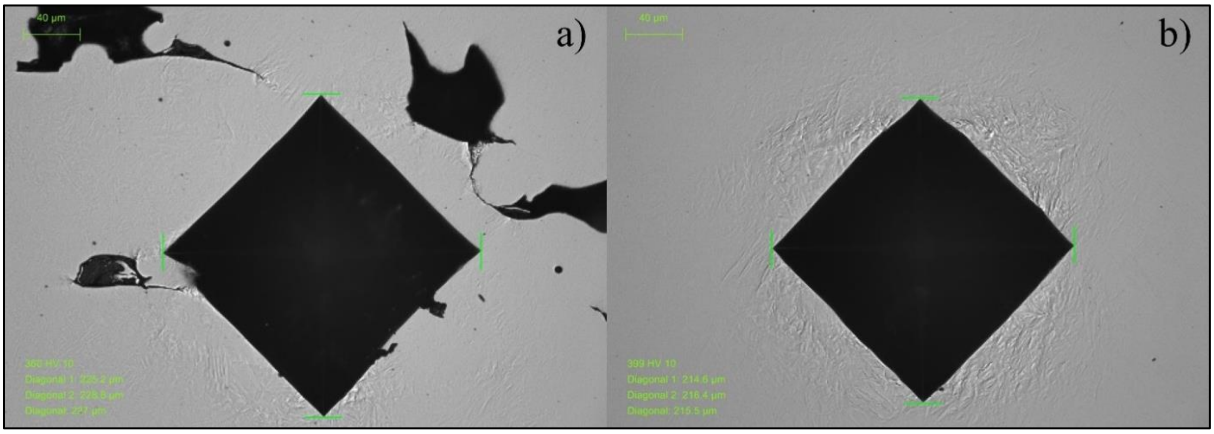

Figure 28. Hardness indentations measured by HV10 at 40.0 J/mm³ a) and 46.7 J/mm³ b) for the 4130 alloy at t=60 µm and P=170 W. Lack-of-fusion is present in a) yielding lower hardness values and large standard deviation compared to the less porous cross section seen in b) at the higher VED.

4.5.2 Hardness of 4140 alloy

The hardness of the 4140 alloy is illustrated in Figure 29. Again, hardness decreased with increased VED and higher laser power yielded lower hardness values due to the increased amount of reheating/tempering. However, the larger carbon content provided a higher hardness (~390-460 HV10) in comparison to the 4130 alloy. An influence of laser power is observed where 210 W and 250 W yielded a more consistent trend compared to 170 W. As mentioned in previous sections, the laser power has an influence on the processing window where higher densities were obtained at lower VED by using a larger laser power. Subsequently, the unclear trend at 170 W between 60-75 J/mm^3 can be correlated to low density (see Figure 20 for comparison), and the vast amount of porosities present influencing hardness indentations.

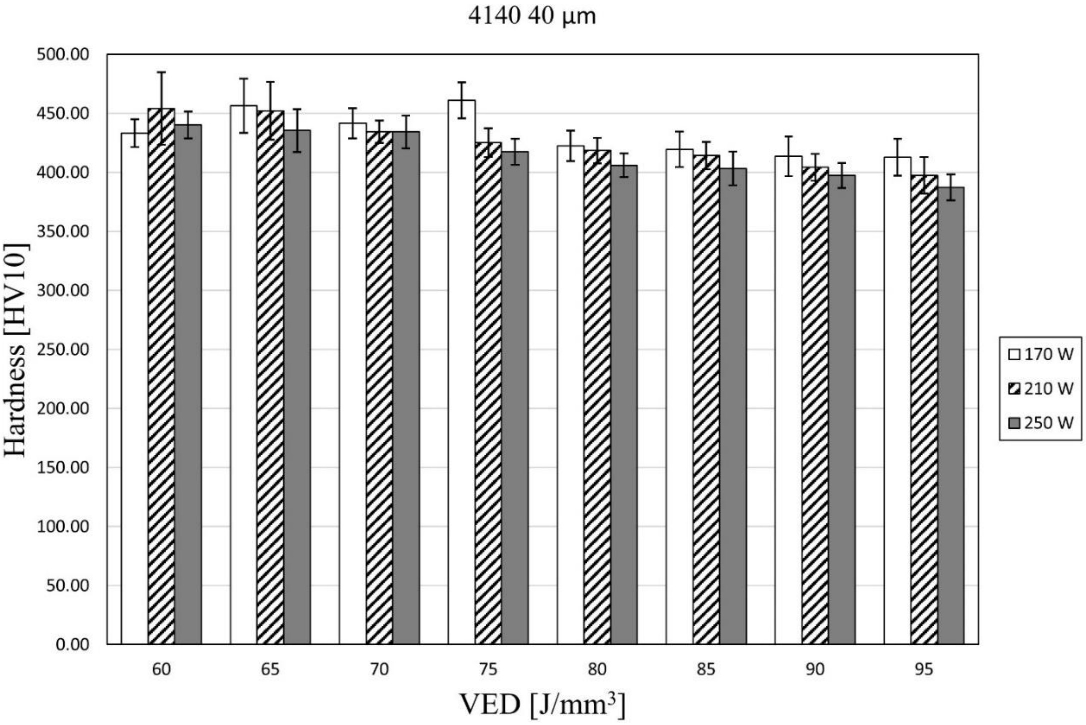

Figure 29. Illustration of the hardness (HV10) evolution with increased VED (J/mm³) and the influence of laser power using 170 (W), 210 (W) and 250 (W) for the 4140 alloy and 40 (µm) layer thickness.

The influence of laser power on the hardness is also seen when increasing the layer thickness to 60 µm. In Figure 30, a rise in hardness (~420-450 HV10) is measured from 40.0 to 50.0 J/mm^3 at the lowest operated laser power with large standard deviations. Compared to the gained processing window in Figure 21, the rapid increase in density could be considered as the reason of the rise in hardness at lower VED. Considering the two larger laser powers, the trends are comparable with what was mentioned earlier where the hardness gradually decreases as the power input increases and the 250 W laser power shows slightly lower hardness compared to the 210 W.

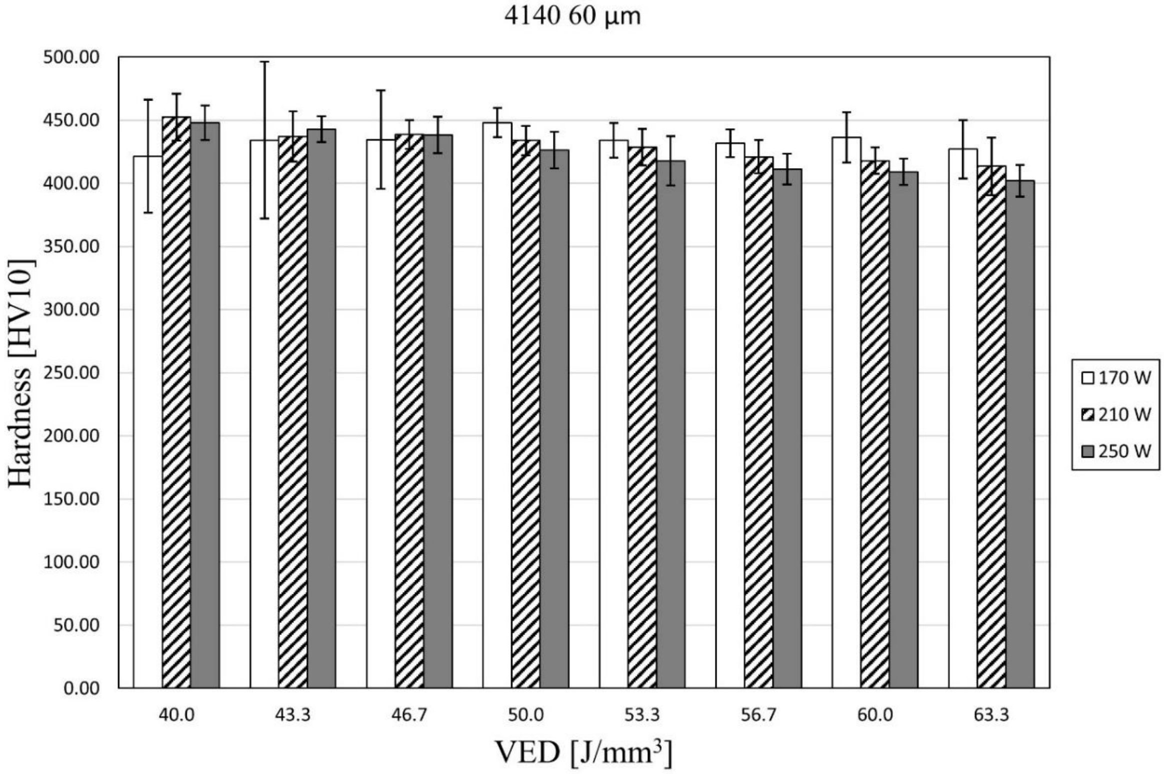

Figure 30. Illustration of the hardness (HV10) evolution with increased VED (J/mm³) and the influence of laser power using 170 (W), 210 (W) and 250 (W) for the 4140 alloy and 60 (µm) layer thickness.

5. Discussion

The location of the processing window, in terms of surface energy density, was found to be highly dependent on the process parameters and the evolution of defects. In the following chapters the influence of layer thickness and laser power on the processing window will be discussed in the context of defects, melt pool characteristics, microstructure and hardness.

5.1 Influence of layer thickness and laser power on the processing window

The influence of layer thickness on the processing window is plotted in Figure 31, including the results from the investigation at a 20 µm layer thickness that was done previously by Steinlechner [28]. By keeping the laser power constant (170 W), similar trends are observed for both alloy systems. The increase in layer thickness shifts the processing window and higher SED is required for high density.

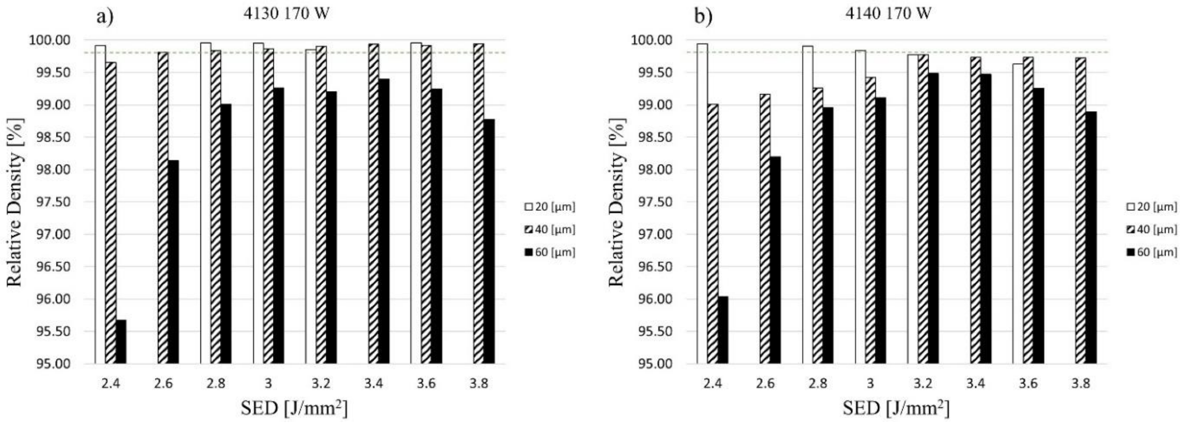

Figure 31. Influence of layer thickness on the processing window 4130 a) and 4140 b) at 170 W. The results for the 20 µm layer thickness were gained by previous work by using the same machine and equivalent SED [28].

The shift of the processing window can be explained by arranging micrographs into a SED versus layer thickness matrix, as illustrated in Figure 32 for the 4130 alloy. The change in defect characteristics from 2.4 to 2.8 J/mm^2 provides an estimation of where this region is located with respect to the processing window. The 20 µm samples show close to no pores present at both energy values while the 40 µm layer thickness exhibits lack-of-fusion and spherical pores at 2.4 J/mm^2 which reduce in numbers and size at 2.8 J/mm^2, yielding a density close to 99.8%. On the contrary, more severe lack-of-fusion is observed at 60 µm at low SED and slightly decreases at 2.8 J/mm^2, indicating that the processing window is located at higher SED values. Thus, the layer thickness has a great influence on the starting energy density as well as the width of the processing window and is characterized by the nature of defects at a certain SED.

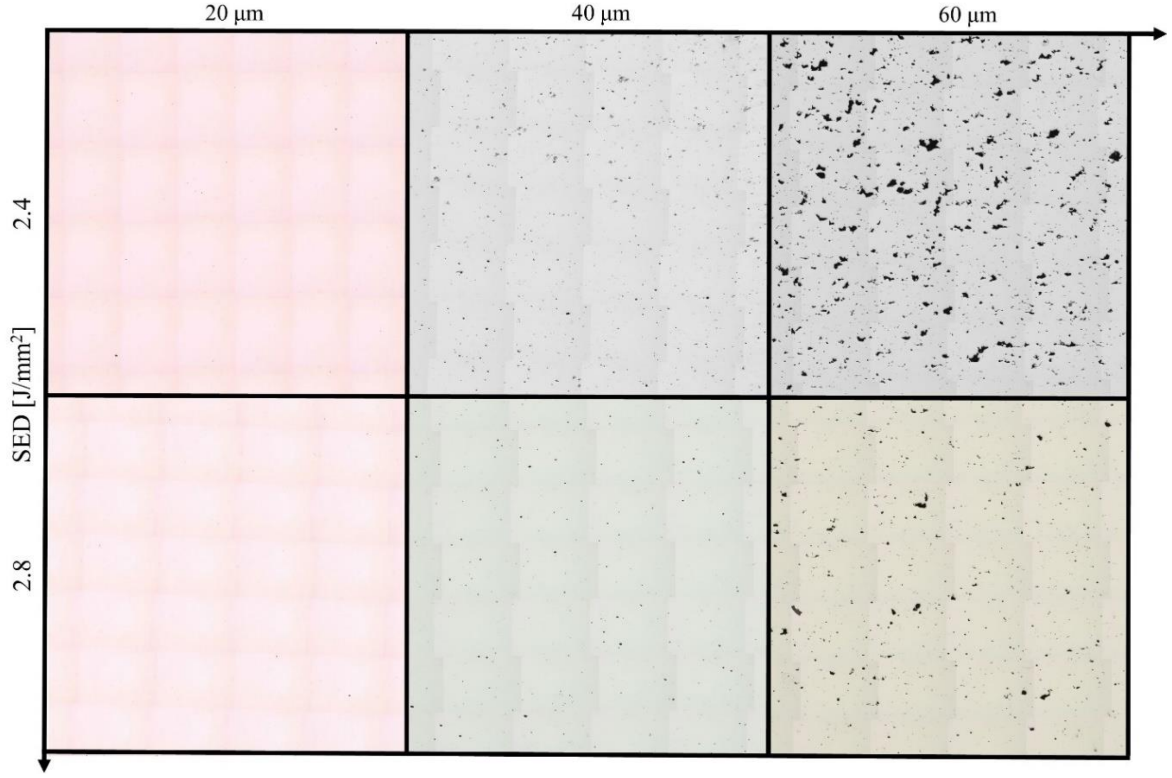

Figure 32. Light optical micrographs, illustrating defect evolution and influence of layer thickness and SED for the 4130 alloy.

The size difference between the lack-of-fusion pores at the different layer thicknesses, needs greater consideration. The results from Section 4.3 showed that the smallest obtained melt pool depth was still 1.8 times larger (~100 μm) than the layer thickness, meaning the melt pool should have been deep enough to provide proper fusion with the previous layer. The great overlap between melt tracks described in Figure 23 further suggests that lack-of-fusion did not occur due to the use of too large hatch spacing. Taking both findings into consideration, it is believed that the lack-of-fusion is a product of melt pool instability. Qiu et al. [21] showed that increased scan speed and layer thickness cause melt flow instabilities resulting in splashing of powder leaving regions of open valleys and protrusions on the surface. They concluded that these valleys would stay within the sample as several layers of penetration is needed to compensate for the increased depth of unmelted material [21]. This might explain the observed lack-of-fusion, where the distance between the bottom of melt pools and the previous layer exceeded the layer thickness. In Figure 33, 4140 etched cross sections are presented. At low SED an increase in melt track instability is observed in the build direction showing larger pores closer to the top layer. In contrast continuous melt tracks are observed at higher SED possibly explained by the removal of this splashing effect that leads to discontinuities of the melt tracks and lack-of-fusion.

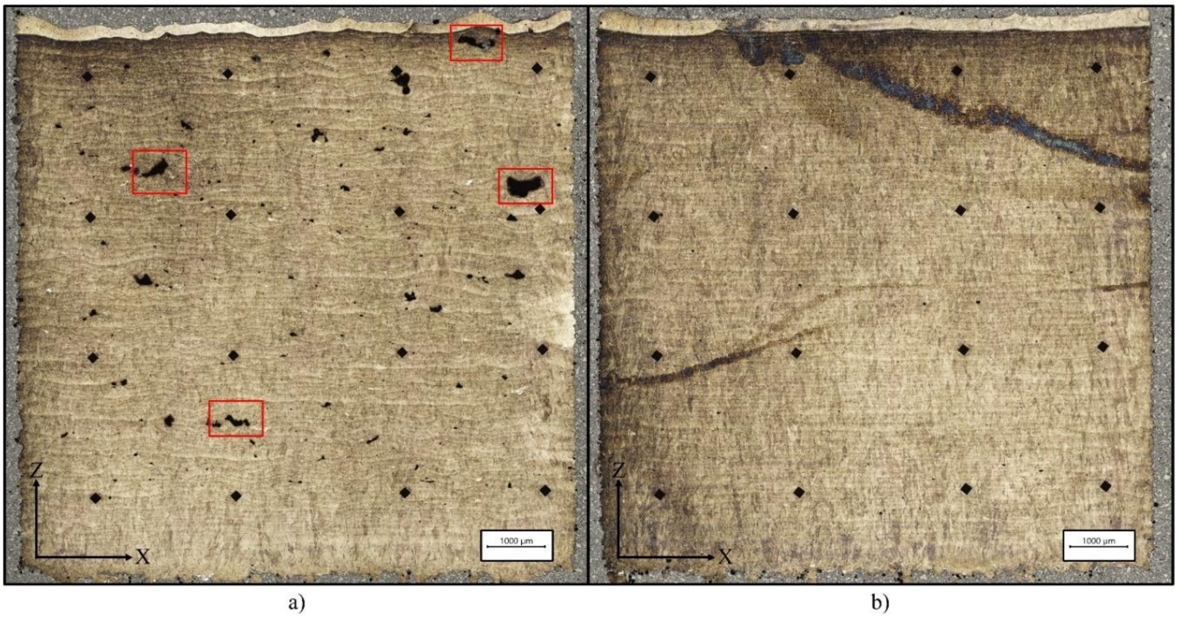

a) b)

Figure 33. Stitched 4140 cross sections etched with 3% Nital (t=60 μm) illustrating melt track instability and increasing size of pores (marked by red squares) along the Z-axis at low SED (2.4 J/mm²) a). The larger pores closer to the top surface in a) can be explained by the increase in amount of material needed to be remelted when valleys are generated as consequence of powder splashing. This is not observed at high SED (3.8 J/mm²) b) where less peaks and valleys are seen at the top surface.

The combined results of Section 4.2 show that the laser power has an influence on the processing window, which is more pronounced at larger layer thickness. Increased laser power shifts the printable region to lower SEDs. Furthermore, a 170 W laser power fails to provide high density at 60 μm layer thickness. Qiu et al. [21] suggested that with an increased layer thickness an increased amount of energy is spent on melting more powder, leaving less energy to spare during the remelting of previous layers. Furthermore, Letenneur et al. [12] showed that the layer thickness can significantly alter the powder bed density and thus the physical properties, such as thermal conductivity of the powder.

5.2 Lack-of-fusion threshold

In literature, studies tend to combine process parameters with melt pool dimensions to explain the occurrence of defects. A commonly used ratio for avoiding lack-of-fusion is melt pool depth D divided by layer thickness (D/t). And it is stated that D/t should be larger than 1 to ensure proper fusion between subsequent layers [23]. This section investigates whether such a condition can be defined for 4130 and 4140 and if there is an influence of laser power and layer thickness on the D/t criterion.

In Figure 34, the influence of D/t on the processing window is presented at the 60 μm layer thickness for 4130. It can be observed that the D/t ratio has a large influence on density. An approximated threshold at D/t=2.7, defined by the vertical red line, marks the transition into 99.8% obtained density. This means that in order to achieve required density, melt pool depths larger than 162 µm are required. This was not achieved for the 170 W, indicating that within the studied SED range higher laser power is needed at 60 µm layer thickness.

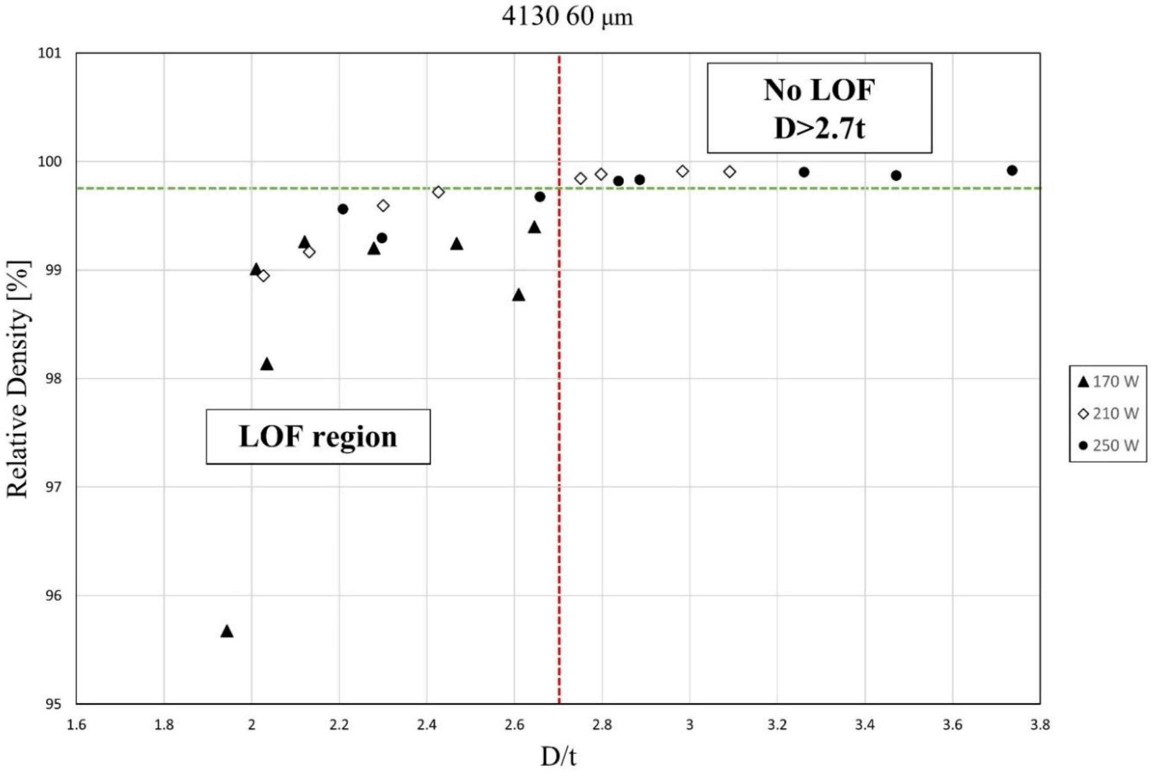

Figure 34. Relative density % and the influence of D/t at 60 and varied laser power for the 4130 alloy.

5.3 The benefit of surface energy density as design parameter when altering layer thickness

SED was shown to be a useful parameter when comparing melt pool characteristics at different layer thicknesses. The melt pool size was similar at the same SED, independent of the layer thickness (see Figure 35). This is valid if the melt pool instabilities discussed in the previous sections are avoided. Thus, due to this ability of SED to provide similar melt pool size regardless of layer thickness, it is easy to study the evolution of defects within the same processing range. This side by side comparison is not possible by using VED as a great alteration of the process parameters is needed to achieve the same VED for different layer thickness (see Section 3.3.1 for a more detailed description). However, it should be noted that the melt pools, see Figure 35, do not provide a perfect estimation of the melt pool geometry. For a better representation of the width and depth it is suggested that single melt tracks are performed to obtain a clear 3D estimation of the melt pool dimensions. Which could strengthen the argument of SED as combined parameter when varying the layer thickness.

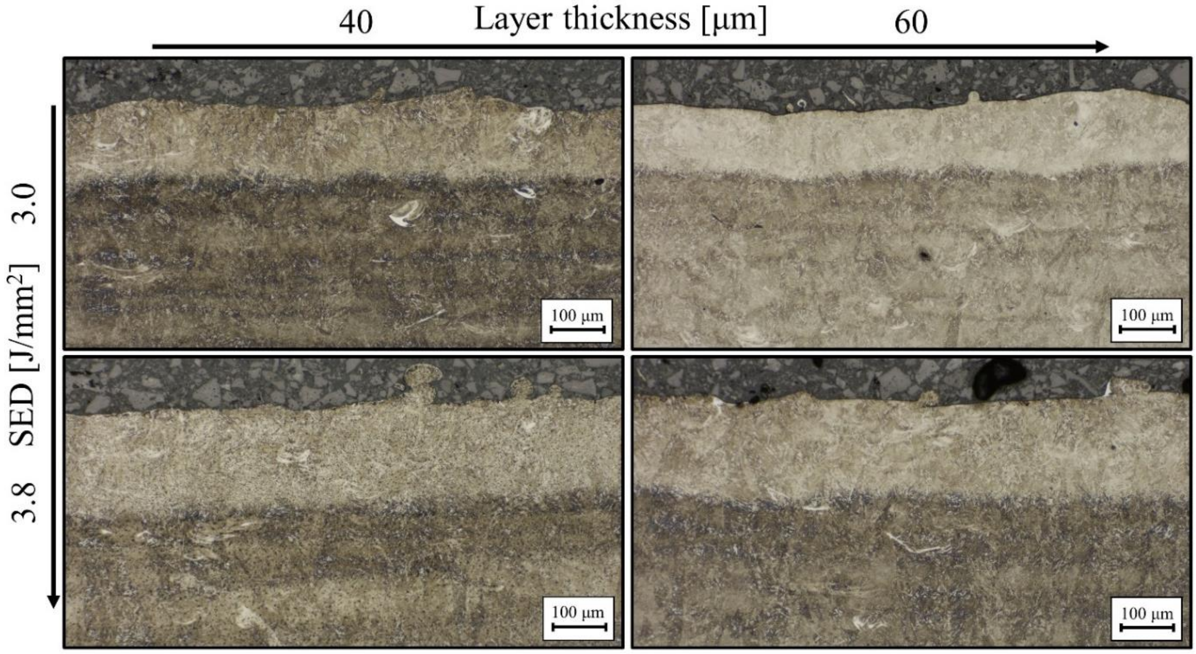

Figure 35. Etched cross sections of the top surface illustrating similarities in melt pool size at the same SED, independent of layer thickness.

5.4 Influence of layer thickness on hardness

In Figure 36, differences in hardness a) and melt pool depth b) at 40 and 60 µm layer thickness is presented for 4130 alloy as functions of VED. Overall, the hardness and melt pool depth have an inverse linear relationship to the supplied VED where the hardness decreases, while the melt pool depth increases. Considering the influence of layer thickness, the hardness values are significantly lower at 60 µm compared to 40 µm at the same VED. This can be explained by the 400 mm/s decrease in scan speed required at 60 µm layer thickness to acquire the same VED as the 40 µm. Consequently, the larger layer thickness is exposed to the laser for longer times resulting in deeper melt pools. With the increase in melt pool depth more material gets remelted and reheated causing a more pronounced tempering of the brittle martensitic laths, reducing its hardness. Damon et al. proposed that this tempering effect with VED stems from lower cooling rates [3]. While the cooling rate might be a part of the cause, it is suggested that the amount of remelting and reheating is the main reason behind this greater tempering effect.

Figure 36 further shows that the choice of laser power has an impact on the hardness. Here, the influence of laser power is opposite for hardness and melt pool depth. As discussed in Sections 4.3 & 4.5 lower hardness and deeper melt pools are gained by operating at a larger laser power. This indicates that the laser power is more influential in lowering the hardness than the exposure time, as the scan speeds were ~250 mm/s higher at each incremental increase of laser power at equal SED and VED.

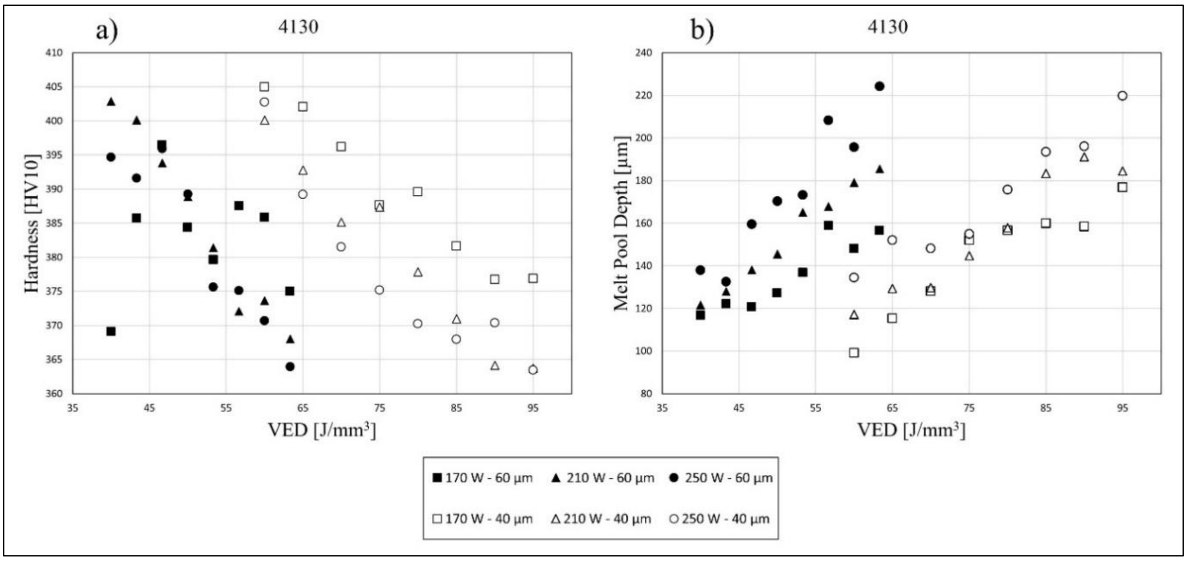

Figure 36. Influence of layer thickness and volumetric energy density on hardness (HV10) a) and melt pool depth in µm b) presented at 170 W, 210 W and 250 W laser power for the 4130 alloy.

The same correlation between hardness and VED at varied layer thickness is observed for the 4140 alloy, illustrated in Figure 37. The major difference is the larger hardness values as opposed to the 4130 alloy, (390-460 HV10 vs 360-405 HV10). It is well known that higher carbon content increases the hardenability. This work found that surface cracking occurred at SEDs <3.0 J/mm^2 which is related to a hardness >420 HV10. This possibly explains why no cracking was observed within the 4130 samples, as the highest obtained hardness was 405 HV10. Thus, to avoid surface cracking it is recommended that the hardness is kept below ~420 HV10, which in the case of 4140 can be controlled by using a 180°C preheating and SEDs above 3.0 J/mm^3.

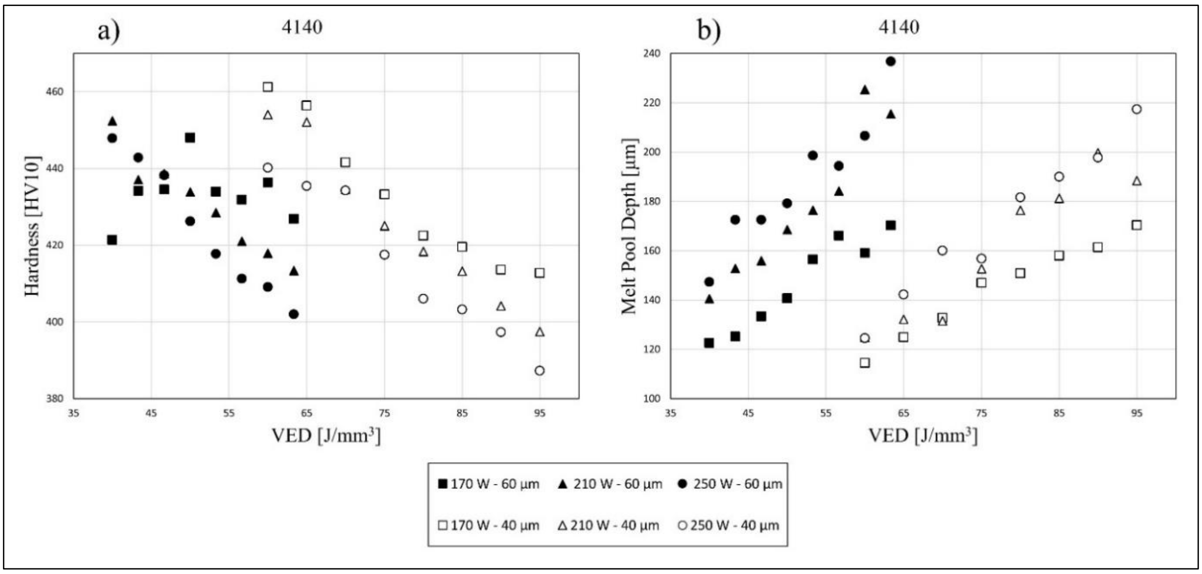

Figure 37. Influence of layer thickness and volumetric energy density on hardness (HV10) a) and melt pool depth µm b) presented at 170 W, 210 W and 250 W laser power for the 4130 alloy.

5.5 Build rate

The low build rate of L-PBF is a major bottleneck and one of the main concerns in making the L-PBF economically justifiable. It was described in literature that there are different ways to define the total productivity of L-PBF. The total build time can be estimated by the Magics software that is integrated with printer (after defining the build volume and the process parameters). It can also be separated into the section of the process where the laser is scanning the surface (build rate) as well as the time required for deposition of a new layer of powder (idle time). The build rate (cm^3/h) can be increased by altering any of the main process parameters e.g. scan speed, hatch spacing and layer thickness. On the other hand, the amount of times needed for recoating the powder is strongly affected by the layer thickness [14]. Therefore, the layer thickness has the largest impact on the total build as it influences all the process related times. This section presents how the layer thickness influences mainly the total build time (Magics software) and build rate (cm^3/h).

Differences in the total build time (in hours) as calculated by the Magics software are presented in Table 4 at varied layer thickness. It is confirmed that by doubling the layer thickness from 20 to 40 µm the overall build time is decreased by 49%. In addition, the build time is further reduced at 60 µm, resulting in a total of 66% reduction relative to the 20 µm layer thickness. These results demonstrate the large impact that layer thickness have on manufacturing times and an increase in thickness can reduce the costs, making L-PBF of 4130 and 4140 a more viable option for industrial use. However, it is also important to consider the influence layer thickness have on density and material properties as mentioned in previous sections.

Table 4. The required build time of each print (h) as estimated by the Magic Software using different layer thicknesses and the percentage of reduced build with increased layer thickness in relation to 20 µm. *Note that the same parameters were used for the supports.*

Layer thickness (µm)	Total build time (h)	Supports only (h)	Reduced build time (%)
20	21.00	0.9	-
40	10.64	0.9	49
60	7.23	0.9	66

In Figure 38, the tradeoff between build rate (cm^3/h) and part density is plotted for all printed samples, separated by layer thickness and laser power. By increasing the layer thickness, maximum build rates of ~18 cm^3/h and ~16 cm^3/h were achieved for the 4130 and 4140 alloys, respectively. Compared to previous established process parameters at 20 µm, the newly developed parameters correspond to an increase in build rate of up to ~165%. However, while we gain higher build rates a small sacrifice must be considered in terms of density. Here, the requirements in quality and cost of the intended component are essential.

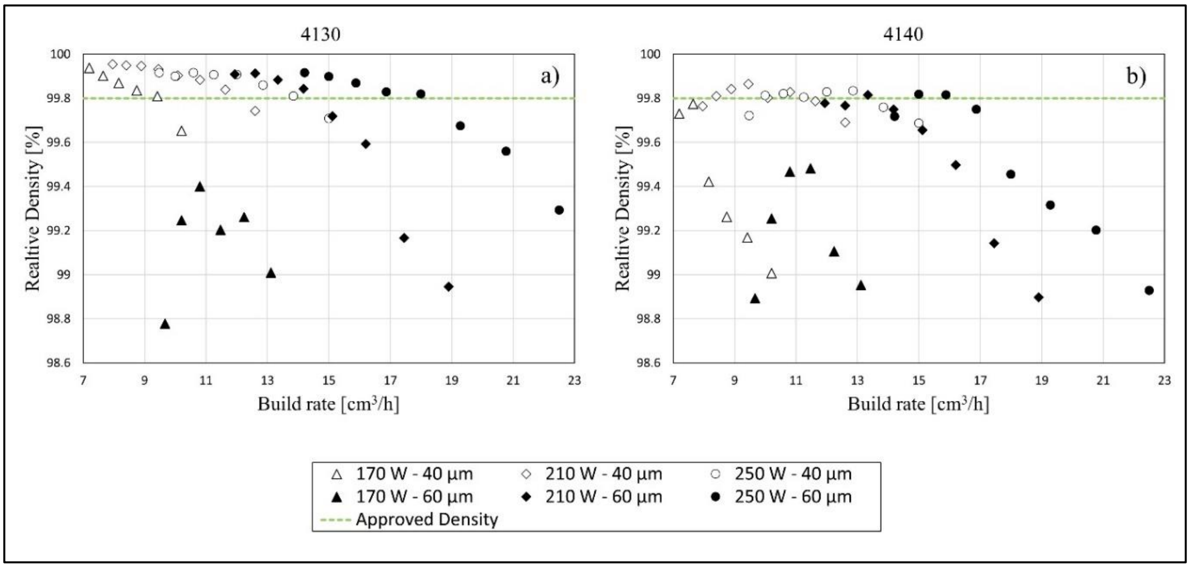

Figure 38. Illustration of the processing window as a function of build rate.

6. Conclusion

This work aimed to improve the build rate of L-PBF low alloy steels by varying the layer thickness. Below follows a list of the main findings as well as recommendations on future research necessary to improve on the knowledge of L-PBF of low alloy steels.

- Processing windows were established for increased layer thicknesses in terms of SED (J/mm^2).
    - 4130: 40 µm (2.6-3.8 J/mm^2) and 60 µm (3.0-3.8 J/mm^2)
    - 4140: 40 µm (2.8-3.6 J/mm^2) and 60 µm (3.4-3.6 J/mm^2)
- Larger layer thickness changes the location of the printable region to higher SED (J/mm^2). The main cause is that more energy is required to prevent powder bed instabilities leading to lack-of-fusion pores. These instabilities can be removed by increasing the SED and/or the laser power.
- Larger layer thickness induces greater sensitivity to the laser power used. This is seen by the greater differences in density between 170 W, 210 W and 250 W at 60 µm compared to 40 µm.
- SED is a beneficial combined parameter when comparing melt pool size between different layer thicknesses. Due to its independence of layer thickness the design of experiment can be performed within a smaller process region compared if designed in terms of VED.
- At equal VED and constant laser power, lower hardness values are obtained at 60 µm layer thickness, compared to components printed at 40 µm. This could be explained by the slower scan speeds that increases the exposure time of the laser.
- Above a SED of 3.0 J/mm^2 corresponding to hardness values below ~420 HV10, no cold cracking was observed in the 4140 alloy regardless of layer thickness.
- It was proven that high density samples can be produced at up to ~165% increased build rate and a reduction in total build time of ~66% compared to printing with 20 µm layer.

6.1 Recommendations for future work

In order to understand the influence of layer thickness in a greater context, mechanical properties of the highest performing parameters of this study should be evaluated in terms of tensile strength, impact toughness and fatigue life. An in-depth study of the microstructure is also recommended by using more advanced techniques such as transmission electron microscopy.

Further, the validity of SED as a design parameter to predict melt pool size at different layer thicknesses should be further investigated. A suggestion is to perform single track experiments (at varied layer thickness and the same SED) to obtain a correct estimation of melt pool/melt track dimensions.

7. References

[1] T. DebRoy, H. L. Wei, J. S. Zuback, T. Mukherjee, J. W. Elmer, J. O. Milewski, A. M. Beese, A. Wilson-Heid, A. De and W. Zhang, "Additive manufacturing of metallic components – Process, structure and properties," *Progress in Materials Science,* vol. 92, pp. 112-224, 2018.

[2] H. Fayazfar, M. Salarian, A. Rogalsky, D. Sarker, P. Russo, V. P. Paserin and E. Toyserkani, "A critical review of powder-based additive manufacturing of ferrous - Process parameters, microstructure and mechanical properties," *Materials and Design,* vol. 144, pp. 98-128, 2018.

[3] J. Damon, R. Koch, D. Kaiser, G. Graf, S. Dietrich and V. Schulze, "Process development and impact of intrinsic heat treatment on the mechanical performance of selective laser melted AISI 4140," *Additive Manufacturing,* vol. 28, pp. 275-284, 2019.

[4] A. Bobel, L. G. Hector, I. Chelladurai, A. K. Sachdev, T. Brown, W. A. Poling, R. Kubic, B. Gould, C. Zhao, N. Parab, A. Greco and T. Sun, "In situ synchrotron X-ray imaging of 4140 steel laser powder bed fusion," *Materialia,* vol. 6, p. 100306, 2019.

[5] W. Wang and S. Kelly, "A Metallurgical Evaluation of the Powder-Bed Laser Additive Manufactured 4140 Steel Material," *JOM,* vol. 68, pp. 869-875, 2016.

[6] X. Li, T. Yong Hao, W. Habimana Jean, P. Wang, W. Lu, M. Cagirici, C. Y. A. Ong, T. S. Herng, J. Wei and J. Ding, "Heterogeneously tempered martensitic high strength steel by selective laser melting and its micro-lattice: Processing, microstructure, superior performance and mechanisms," *Materials & Design,* vol. 178, p. 107881, 2019.

[7] E. Jelis, M. Hespos, S. L. Groeschler and R. Carpenter, "L-PBF of 4340 Low Alloy Steel: Influence of Feedstock Powder, Layer Thickness, and Machine Maintenance," *Journal of Materials Engineering and Performance,* vol. 28, no. 2, pp. 693-700, 2018.

[8] E. Jelis, M. R. Hespos and N. M. Ravindra, "Process Evaluation of AISI 4340 Steel Manufactured by Laser Powder Bed Fusion," *Journal of Materials Engineering and Performance,* vol. 1, no. 27, pp. 63-71, 2017.

[9] S. Mannan and F. P. Lees, "Chapter 12 - Pressure System Design," in *Lees' Loss Prevention in the Process Industries*, 4 ed., Amsterdam, Elsevier Butterworth-Heinemann, 2012, pp. 509-617.

[10] D. Herzog, V. Seyda, E. Wycisk and C. Emmelmann, "Additive manufacturing of metals," *Acta Materialia,* vol. 117, pp. 371-392, 2016.

[11] J. Oliveira, A. LaLonde and J. Ma, "Processing parameters in laser powder bed fusion metal additive manufacturing," *Materials & Design,* vol. 193, p. 108762, 2020.

[12] M. Letenneur, A. Kreitcberg and V. Brailovski, "Optimization of Laser Powder Bed Fusion Processing Using a Combination of Melt Pool Modeling and Design of Experiment Approaches: Density Control," *Journal of Manufacturing and Materials Processing,* vol. 3, no. 1, pp. 1-13, 2019.

[13] A. Haider, H. Ghadbeigi and K. Mumtaz, "Processing Parameter Effects on Residual Stress and Mechanical Properties of Selective Laser Melted Ti6Al4V," *Journal of Materials Engineering and Performance,* vol. 27, no. 8, pp. 4059-4068, 2018.

[14] M. Kniepkamp, J. Harbig, C. Seyfert and E. Abele, "Towards high build rates: Combining different layer thicknesses within one part in selective laser melting," in *Solid Freeform Fabrication 2018: Proceedings of the 29th Annual International*, Texas, 2018.

[15] U. Scipioni Bertoli, A. J. Wolfer, M. J. Matthews, J.-P. R. Delplanque and J. M. Schoenung, "On the limitations of Volumetric Energy Density as a design parameter for Selective Laser Melting," *Materials & Design,* vol. 113, pp. 331-340, 2017.

[16] S. L. Campanelli, N. Contuzzi, P. Posa and A. Angelastro, "Printability and Microstructure of Selective Laser Melting of WC/Co/Cr Powder," *Materials,* vol. 12, no. 15, p. 2397, 2019.

[17] I. Yadroitsev, A. Gusarov, I. Yadroitsava and I. Smurov, "Single track formation in selective laser melting of metal powders," *Journal of Materials Processing Technology,* vol. 210, no. 12, pp. 1624-1631, 2010.

[18] S. Antonella and A. Nouri, "Microstructural porosity in additive manufacturing: The formation and detection of pores in metal parts fabricated by powder bed fusion," *Journal of Advanced Manufacturing and Processing,* vol. 1, no. 3, 2019.

[19] D. Zhang, S. Sun, D. Qiu, M. A. Gibson, M. S. Dargusch, M. Brandt, M. Qian and M. Easton, "Metal Alloys for Fusion-Based Additive Manufacturing," *Advanced Engineering Materials,* vol. 20, no. 5, p. 1700952, 2018.

[20] S. Sun, M. Brandt and M. Easton, "2 - Powder bed fusion processes: An overview," in *Laser Additive Manufacturing: Materials, Design, Technologies, and Applications*, RMIT University, Centre for Additive Manufacturing, Melbourne, VIC, Australia, Woodhead Publishing, 2017, pp. 55-77.

[21] C. Qiu, C. Panwisawas, M. Ward, H. C. Basoalto, J. W. Brooks and M. M. Attallah, "On the role of melt flow into the surface structure and porosity development during selective laser melting," *Acta Materialia,* vol. 96, pp. 72-79, 2015.

[22] R. Mertens, B. Vrancken, N. Holmstock, Y. Kinds, J.-P. Kruth and J. Van Humbeeck, "Influence of Powder Bed Preheating on Microstructure and Mechanical Properties of H13 Tool Steel SLM Parts," *Physics Procedia,* vol. 83, pp. 882-890, 2016.

[23] R. Seede, D. Shoukr, B. Zhang, A. Whitt, S. Gibbons, P. Flater, A. Elwany, R. Arroyave and I. Karaman, "An ultra-high strength martensitic steel fabricated using selective laser melting additive manufacturing: Densification, microstructure, and mechanical properties," *Acta Materialia,* vol. 186, pp. 199-214, 2020.

[24] Z. Sun, X. Tan, S. B. Tor and W. Y. Yeong, "Selective laser melting of stainless steel 316L with low porosity and high build rates," *Materials & Design,* vol. 104, pp. 197-204, 2016.

[25] S. Shamsdini, S. Shakerin, A. Hadadzadeh, B. S. Amirkhiz and M. Mohammadi, "A trade-off between powder layer thickness and mechanical properties in additively manufactured maraging steels," *Materials Science and Engineering: A,* vol. 776, p. 139041, 2020.

[26] P. Bajaj, A. Hariharan, A. Kini, P. Kürnsteiner, D. Raabe and E. Jägle, "Steels in additive manufacturing: A review of their microstructure and properties," *Materials Science & Engineering A,* vol. 772, p. 138633, 2020.

[27] R. Singh, "Classification of steels," in *Applied Welding Engineering - Processes, Codes, and Standards*, 2 ed., Oxford, Butterworth-Heinemann , 2016, pp. 57-64.

[28] R. Steinlechner, "Development of Laser Powder Bed Fusion parameters and their effect on microstructure formation in Low Alloyed Steels," Techische universität Wien , Wien, 2020.

[29] M. Orme, I. Madera, M. Gschweitl and M. Ferrari, "Topology Optimization for Additive Manufacturing as an Enabler for Light Weight Flight Hardware," *Designs,* vol. 2, p. 51, 2018.

[30] H. Zheng, H. Li, L. Lang, S. Gong and Y. Ge, "Effects of scan speed on vapor plume behavior and spatter generation in laser powder bed fusion additive manufacturing," *Journal of Manufacturing Processes,* vol. 36, pp. 60-67, 2018.

[31] S. A. Khairallah, A. T. Anderson, A. Rubenchik and W. E. King, "Laser powder-bed fusion additive manufacturing: Physics of complex melt flow and formation mechanisms of pores, spatter, and denudation zones," *Acta Materialia,* vol. 108, pp. 36-45, 2016.

[32] "2 - Powder bed fusion processes: An overview," in *Laser Additive Manufacturing: Materials, Design, Technologies, and Applications*, RMIT University, Centre for Additive Manufacturing, Melbourne, VIC, Australia, Woodhead Publishing, 2017, pp. 55-77.